

ELG Spectroscopic Systematics Analysis of the DESI Data Release 1

J. Yu¹, A. J. Ross^{2,3,4}, A. Rocher^{1,5}, O. Alves⁶, A. de Mattia⁵,
 D. Forero-Sánchez¹, J. Kneib^{1,7}, A. Krolewski^{8,9,10}, T.-W. Lan¹¹,
 M. Rashkovetskyi¹², J. Aguilar¹³, S. Ahlen¹⁴, S. Bailey¹³,
 D. Brooks¹⁵, E. Chaussidon¹³, T. Claybaugh¹³, A. de la Macorra¹⁶,
 Arjun Dey¹⁷, Biprateep Dey¹⁸, P. Doel¹⁵, K. Fanning^{19,20},
 J. E. Forero-Romero^{21,22}, E. Gaztañaga^{23,24,25}, S. Gontcho A
 Gontcho¹³, K. Honscheid^{2,26,4}, C. Howlett²⁷, S. Juneau¹⁷,
 T. Kisner¹³, A. Kremin¹³, A. Lambert¹³, M. Landriau¹³,
 L. Le Guillou²⁸, M. E. Levi¹³, M. Manera^{29,30}, P. Martini^{2,3,4},
 A. Meisner¹⁷, R. Miquel^{31,30}, J. Moustakas³², E. Mueller³³,
 A. Muñoz-Gutiérrez¹⁶, A. D. Myers³⁴, J. Nie³⁵, G. Niz^{36,37},
 N. Palanque-Delabrouille^{5,13}, W. J. Percival^{8,9,10}, C. Poppett^{13,38,39},
 F. Prada⁴⁰, M. Rezaie⁴¹, G. Rossi⁴², E. Sanchez⁴³,
 E. F. Schlafly⁴⁴, D. Schlegel¹³, M. Schubnell^{45,6}, H. Seo⁴⁶,
 D. Sprayberry¹⁷, G. Tarlé⁶, B. A. Weaver¹⁷, P. Zarrouk²⁸,
 C. Zhao⁴⁷, R. Zhou¹³, H. Zou³⁵

Affiliations are in Appendix C

E-mail: jiaxi.yu@epfl.ch

Abstract. Dark Energy Spectroscopic Instrument (DESI) uses more than 2.4 million Emission Line Galaxies (ELGs) for 3D large-scale structure (LSS) analyses in its Data Release 1 (DR1). Such large statistics enable thorough research on systematic uncertainties. In this study, we focus on spectroscopic systematics of ELGs. The redshift success rate (f_{goodz}) is the relative fraction of secure redshifts among all measurements. It depends on observing conditions, thus introduces non-cosmological variations to the LSS. We, therefore, develop the redshift failure weight (w_{zfail}) and a per-fibre correction (η_{zfail}) to mitigate these dependences. They have minor influences on the galaxy clustering. For ELGs with a secure redshift, there are two subtypes of systematics: 1) catastrophics (large) that only occur in a few samples; 2) redshift uncertainty (small) that exists for all samples. The catastrophics represent 0.26% of the total DR1 ELGs, composed of the confusion between [O II] and sky residuals, double objects, total catastrophics and others. We simulate the realistic 0.26% catastrophics of DR1 ELGs, the hypothetical 1% catastrophics, and the truncation of the contaminated $1.31 < z < 1.33$ in the ABACUSUMMIT ELG mocks. Their P_ℓ show non-negligible bias from the uncontaminated mocks. But their influences on the redshift space distortions (RSD) parameters are smaller than 0.2σ . The redshift uncertainty of DR1 ELGs is 8.5 km s^{-1} with a Lorentzian profile. The code for implementing the catastrophics and redshift uncertainty on mocks can be found in https://github.com/Jiaxi-Yu/modelling_spectro_sys.

Contents

1	Introduction	1
2	Data and Mocks	3
2.1	DESI DR1 Data	3
2.1.1	Redshift Success Rate f_{goodz}	3
2.1.2	Repeated Observation Catalogue	4
2.2	Galaxy Mocks and Covariance Matrices	4
3	Method	5
3.1	Two-point Statistics	5
3.2	Quantifying the Clustering Differences	6
3.3	RSD Tests: ShapeFit and Full Modelling	7
4	Redshift Success Rate Corrections	7
4.1	The Redshift Failure Weight w_{zfail}	7
4.1.1	[O II] Emission and Redshift Measurement	8
4.1.2	The f_{goodz} Model and w_{zfail} Weight	9
4.2	The Focal Plane Correction η_{zfail}	10
4.3	Performances of w_{zfail} and η_{zfail}	12
5	Redshift Catastrophics and Redshift Uncertainty	14
5.1	Characterising the Catastrophics	15
5.2	Modelling the Catastrophics	17
5.3	Impact of Catastrophics	18
5.4	Redshift Uncertainty	21
6	Conclusion	22
A	Visualise Spectra of ELG Catastrophics	24
B	Catastrophics Impacts on Small-Scale 2PCF	24
C	Author Affiliations	24

1 Introduction

Galaxy redshift surveys probe the 3D LSS of the Universe by measuring the redshifts of millions of galaxies and quasars. Baryonic acoustic oscillations (BAO; [1]) and redshift-space distortions (RSD; [2]) encoded in the galaxy clustering reflect the properties of dark energy and dark matter. However, artefacts, or observational systematics, may introduce biases or reduce the precision of the cosmological measurements via BAO and RSD [e.g., 3–7]. Therefore, identifying, describing, and correcting any systematics that may exist in the cosmological measurements is essential for redshift surveys.

Dark Energy Spectroscopic Instrument (DESI, 2021-2026) [8–10] is conducting the largest galaxy redshift survey to date with the 4-meter Mayall Telescope at Kitt Peak, Arizona, US. DESI

has already observed thousands of square degrees of the sky using robotic-controlled fibres [11]. It is on track to obtain the spectra of ~ 40 million galaxies and quasars over $14,000 \text{ deg}^2$ of the sky. Its early data release in June 2023 (EDR¹, [12]) published the data collected during the survey validation phase [13] from December 2020 to May 2021, covering several hundred square degrees of sky. Its 5-year survey then started in May 2021, and the data collected during the first year of observations will be made available in the first data release (DR1, [14]). DR1 uses 300,017 Bright Galaxies between redshift $0.1 < z < 0.4$ (BGS; [15]), 2,138,600 Luminous Red Galaxies between redshift $0.4 < z < 1.1$ (LRGs; [16]), 2,432,022 Emission Line Galaxies between redshift $0.8 < z < 1.6$ (ELG; [17]) and 1,223,170 quasars (QSO) between redshift $0.8 < z < 3.5$ [18] that are observed over more than 7400 deg^2 of the sky for cosmological analysis [19]. These dark matter tracers are grouped into LSS catalogues with different weights [20], aiming at providing unbiased clustering of galaxies, quasars, and the Ly α forest [19, 21]. Accurate estimations of the full covariance matrices [22–26] and data blinding [27] are also crucial for the robustness of the cosmological results. The percent-level precision measurements of BAO are presented in [21, 28], where we show that the BAO precisions of the 1-year DESI observation outperform those from the two-decadal Sloan Sky Digital Survey (SDSS²; [29]). The RSD measurements of DR1 will come very soon in [30]. The cosmological constraints on Ω_m , H_0 , Ω_K , M_ν and dark energy equation of state informed by BAO are concluded in [31], presenting a 3σ detection of a w_0w_a CDM cosmology compared with the Λ CDM. The cosmological constraints from RSD and the measurements of primordial non-Gaussianity f_{NL} will be introduced in [32, 33].

For DESI DR1, we consider three types of observational systematics that could influence the cosmological measurements: target selection [34], fibre assignment [35] and redshift measurements [36, 37]. DESI Legacy Imaging Survey [38] was built to provide galaxy and quasar candidates for spectroscopic observations. The Beijing-Arizona Sky Survey (G, R bands), and the Mayall Z-band Legacy Survey (BASS/MzLS; [39]) comprise the north galactic cap of the DESI footprint with declination larger than 32.375° . The rest of the DESI footprint is covered by the Dark Energy Camera Legacy Survey (DECaLS; [40]) and the Dark Energy Survey (DES; [41]) observed with the Dark Energy Camera (DECam; [42]). The systematics analyses of the redshift measurements are thus split into BASS/MzLS and DECam parts due to the difference in their instruments. Imaging systematics are artefacts introduced from the target selection by, for example, the accuracy of the photometric information and the selection criteria. The modelling and corrections of imaging systematics are described in detail in [43–46]. Fibre assignment with proper designs ensures that the redshift survey will be completed on time but will also introduce unphysical variations in the observed galaxy clustering. [47–50] address the effects of it from different aspects. [51] and this paper characterize the impact of bad redshift measurements for all types of tracers. Specifically, this paper focuses on ELGs, the largest group of objects in the DESI survey, due to their unique role in probing the LSS in the star-forming epoch at $1 < z < 2$.

The success rate of the redshift measurement (f_{goodz}) varies with observing conditions, reflecting the unphysical galaxy density variations brought by the instruments of DESI. Correcting these effects requires fair up- or down-weighting on galaxy samples with secure redshift measurements, thus avoiding potential impact on the LSS analysis. For those with *secure* redshift measurements, their redshift are not necessarily the *true* redshift. A small fraction of ELGs, e.g., $\sim 0.3\%$ for eBOSS DR16 [5] and DESI preliminary studies [17, 52], have *secure* redshifts that are very different from its *true* redshift for various reasons. This may also introduce bias to the clustering measurements by significantly altering the LSS. In most cases, *secure* redshift measurements are close to its *true*

¹<https://data.desi.lbl.gov/doc/releases/edr>

²<https://www.sdss4.org/science/final-bao-and-rsd-measurements/>

redshift, with statistical uncertainties. It is as small as 10 km s^{-1} for DESI ELGs [17, 53], resulting in negligible clustering impact on $s > 5 h^{-1} \text{ Mpc}$. We will study all three aspects of the spectroscopic systematics for DR1 ELGs at $0.8 < z < 1.6$ and quantify their clustering and cosmological impacts.

This paper is arranged as follows. We describe the DR1 data, especially the corrections on the redshift success rate, galaxy mocks, and covariance matrices involved in our systematics analysis in Section 2. The two-point clustering estimators and DESI cosmological pipeline will be introduced in Section 3. Section 4 presents the characterization and corrections of the redshift failures. The feature and impact of redshift catastrophics and uncertainty of ELGs with reliable redshift measurements will be introduced in Section 5. Finally, we conclude our findings in Section 6.

In this work, we adopt a flat ΛCDM fiducial cosmology from the mean results of Planck [54] `BASE_PLIKHM_TTTEEE_LOWL_LOWE_LENSING` with $\omega_b = 0.02237$, $\omega_{\text{cdm}} = 0.12$, $h = 0.6736$, $A_s = 2.083 \cdot 10^{-9}$, $n_s = 0.9649$, $\sigma_8 = 0.8079$, $N_{\text{eff}} = 3.044$, $\sum m_\nu = 0.06 \text{ eV}$ (single massive neutrino). This is the fiducial DESI cosmology when converting the positions of objects to Cartesian coordinates in the two-point statistics computation, and also the cosmology of ELG mocks [55] built on `ABACUSSUMMIT` simulations [56].

2 Data and Mocks

2.1 DESI DR1 Data

The DR1 data of DESI is the first year of the DESI Main Survey (May 2021 to June 2022, [14]). Covering over 7,400 square degrees of the sky, DR1 includes more than 6 million spectra of galaxies and quasars with accurate redshift at $0.1 < z < 3.5$ for cosmological measurements with LSS. We focus on the spectroscopic systematics of `ELG_LOPnotqso` samples (ELG hereafter) in DESI DR1 [20]. This corresponds to ELG targets that have a high observational priority (`ELG_LOP` with a surface number density $\approx 1940 \text{ deg}^{-2}$) and are not part of QSO targets ($\approx 5\%$ of `ELG_LOP`) [17]. We include three types of data products in our study: 1) the `full_HPmapcut` catalogue that includes all DR1 ELG targets with a good observing prerequisite and imaging properties [19]. It means that all observed ELG targets (not necessarily true ELGs) with good and failed redshift measurements at all redshifts are included. This catalogue is used to construct w_{zfail} (Section 4.1) and explore the possible improvement of it (Section 4.2). We refer to it as `full` catalogue afterwards; 2) the DR1 ELG LSS catalogues with ELGs at $0.8 < z < 1.6$ [20]. It includes the total observational systematics weight w_{tot} , assuming systematics are decomposable and all corrections are non-overlapping. w_{tot} is obtained as follows [19, 20]:

$$w_{\text{tot}} = w_{\text{comp}} w_{\text{sys}} w_{\text{zfail}}, \quad (2.1)$$

where w_{comp} is for the correction of the target completeness due to fibre assignment, w_{sys} is to correct the target density fluctuation existing in the BASS/MzLS and DECam imaging surveys (see [19] for more details), and w_{zfail} is for the failed-redshift systematics (see Section 4.1). The LSS catalogue of ELGs is used to quantify the clustering impact of the redshift failure weight w_{zfail} and its corrections; 3) spectroscopically confirmed ELGs from the One-Percent Survey of EDR. This dataset will be used to construct a catalogue of repeated observation (Section 2.1.2) for systematics studies in Section 5 and provide the visual inspection of catastrophics in Appendix A.

2.1.1 Redshift Success Rate f_{goodz}

w_{zfail} are weights that account for missing objects in the observed LSS (i.e., not in LSS catalogues) due to failed redshift measurements. An ELG redshift measurement is classified as successful if it

meets the requirement as follows [17]

$$\log_{10}(S_{[\text{O II}]}) + 0.2\log_{10}(\Delta\chi^2) > 0.9, \quad (2.2)$$

where $(S_{[\text{O II}]})$ is the signal-to-noise ratio (SNR) of the $[\text{O II}]$ emission line fit, and $\Delta\chi^2$ is the χ^2 difference between the best-fit redshift and the second-best redshift in the REDROCK pipeline. This means that a reliable ELG redshift measurement should have either a high $[\text{O II}]$ SNR or a large $\Delta\chi^2$.

The success rate of redshift measurement is the complement of the redshift failure rate. We always use the normalized redshift success rate f_{goodz} in this study, defined as

$$f_{\text{goodz}}(x) = \frac{N_{\text{goodz}}(x)/N_{\text{obs}}(x)}{\sum^x N_{\text{goodz}}(x)/\sum^x N_{\text{obs}}(x)}, \quad (2.3)$$

where x represents different observing conditions (e.g., the effective observing time, the position on the focal plane). N_{obs} is the number of ELG targets observed in appropriate conditions with no instrumental issue, and N_{goodz} is a subsample of N_{obs} with good redshift measurements (Eq. (2.2)). For DR1 ELGs, $\sum^x N_{\text{goodz}}(x)/\sum^x N_{\text{obs}}(x) = 72.6\%$ [51].

We remind our readers that we measure f_{goodz} for BASS/MzLS and DECam footprint separately. It means that all f_{goodz} studies and discussions are divided into these two areas (i.e., area selections are applied on both N_{goodz} and N_{obs}). Additional selections (e.g., on redshift range as discussed in Figure 2) should be implemented on $N_{\text{goodz}}(x)$ only as they have reliable properties including redshift measurements.

2.1.2 Repeated Observation Catalogue

The studies of redshift catastrophics and uncertainty are based on repeated observations of the same object. The DESI One-Percent Survey, part of the survey validation program [13], has a footprint that overlaps with the DR1 footprint. In DR1, the same object can be observed repeatedly on different nights. So, we select all repeated redshift measurements of ELG_LOPnotqso samples (DR1 ELGs hereafter) by cross-match these two data sets processed with the same versions of REDROCK [37], and we compute the redshift difference $\Delta v = \Delta z c / (1 + z)$ iteratively among pairs. Studies based on these repeated observations represent the properties of DESI DR1 ELGs since they are fair subsamples by construction (see, e.g. Section 5.1)

There are 115,160 pairs of repeated observation for DR1 ELGs, and 307 pairs (0.26%) of them have $|\Delta v| > 1000 \text{ km s}^{-1}$, which are the catastrophics in our study. This is similar to the ELG catastrophics rate of the DESI survey validation data [17]. We will provide a detailed description of these samples in Section 5.1. Pairs with $|\Delta v| < 1000 \text{ km s}^{-1}$ will be used to study the redshift uncertainty (Section 5.4). Δv is roughly symmetric w.r.t. 0 as illustrated in Section 5.4.

2.2 Galaxy Mocks and Covariance Matrices

We employ galaxy mocks that mimic the DR1 ELG samples to assist our study of spectroscopic systematics. The model ELGs were generated by implementing a modified high-mass-quenched HOD model [55] on ABACUS-SUMMIT simulations [56] in a $2 h^{-3} \text{ Gpc}^3$ box at $z = 1.100$. Next, these model galaxies in simulation boxes were downsampled to the observed redshift distribution $n(z)$ of DR1 ELG samples and truncated to a spherical shell that matches the footprint of the DESI DR1 survey. The survey-like model ELGs then went through the data reduction pipeline of real observations [48] (i.e., `almtmt1`) to select the ‘observed’ ELGs. The output mock ELG catalogue is similar to the full catalogue as mentioned in Section 2.1, and we will apply the modelled spectroscopic systematics (see Section 5) to this catalogue. Finally, mocks with and without systematics will be processed by the

pipeline to generate LSS catalogues for data (data type 2 in Section 2.1) and to calculate the two-point statistics (see Section 3.1) for comparison. There are 25 realizations of ABACUS_{SUMMIT} simulations. Therefore, we will implement the systematics on all 25 realizations of the ELG mocks, and their averaged clustering will be used for cosmological tests to reduce the effect of cosmic variance.

The cosmological measurements require accurate estimations of the overall cosmic variance, i.e. the full covariance matrices. We also need accurate covariance matrices to quantify the clustering and cosmological impact of spectroscopic systematics. In our study, we use analytical covariances created by THECOV³ [24] in the Fourier space for the power spectrum multipoles, $P_\ell(k)$, which is based on COVAPT⁴ [57] and RASCALC^{5,6} in the configuration space for the two-point correlation function (2PCF) multipoles, $\xi_\ell(s)$ [25, 58]. We direct the reader to [26] for a detailed study of the covariance matrices in DESI DR1.

3 Method

3.1 Two-point Statistics

Two-point statistics describe the probability of finding excess pairs of galaxies compared to a random distribution. The detailed description of the computation in DESI DR1 can be found in [19]. In this section, we provide a summary of their computational techniques.

The distribution of galaxies from LSS catalogues has been corrected by w_{tot} to screen the impact of observational systematics. In addition, the evolution of the galaxy number density as redshift will introduce extra clustering variance at BAO scale [59]. We thus include the FKP weights w_{FKP} in the clustering measurement, defined as

$$w_{\text{FKP}} = \frac{1}{1 + n_{\text{local}}(z)P_0}, \quad (3.1)$$

where $n_{\text{local}}(z)$ is the tracer average number density at redshift z , and $P_0 = 4000 h^{-3} \text{Mpc}^3$ for ELGs, is the amplitude of the observed power spectrum at $k_0 \approx 0.15 h \text{Mpc}^{-1}$. Therefore, we weight each galaxy with $w_{\text{tot}}w_{\text{FKP}}$ for 2-point statistics measurements.

In the configuration space, we measure the two-point correlation function ξ (2PCF). It depends on the comoving distance s between pairs of galaxies and μ , which is the cosine of the angle between the distance vector s and the line-of-sight. For galaxies observed from redshift surveys, we use the Landy–Szalay estimator (LS) to calculate the ξ [60]:

$$\xi_{\text{LS}} = \frac{\text{DD} - 2\text{DR} + \text{RR}}{\text{RR}}, \quad (3.2)$$

where DD, DR and RR represent the number of galaxy pairs identified in data–data catalogues, data–random catalogues, and random–random catalogues at a given distance and angle (s, μ) normalized by their corresponding total number of pairs in these catalogues. $\xi(s, \mu)$ can be decomposed by Legendre polynomials $L_\ell(\mu)$ to obtain the multipoles of ξ as

$$\xi_\ell(s) = \frac{2\ell + 1}{2} \int_{-1}^1 \xi(s, \mu) L_\ell(\mu) d\mu. \quad (3.3)$$

³<https://github.com/cosmodesi/thecov>

⁴<https://github.com/JayWadekar/CovAPT/>

⁵<https://github.com/oliverphilcox/RascalC>

⁶<https://github.com/misharash/RascalC-scripts/>

We compute the galaxy pairs for observations using the DESI package `PYCORR`⁷, a wrapper of the `CORRFUNC` package [61, 62], between 0–200 h^{-1} Mpc in 200 linear bins and with 200 linear μ bins and regroup them to obtain the ξ_ℓ with $\Delta s = 4 h^{-1}$ Mpc for $\ell = 0, 2, 4$. We use the comoving distance at $s \in [30, 200] h^{-1}$ Mpc for χ^2 calculations (Section 3.2).

Power spectra $P(k)$ are two-point statistics in Fourier space. Its estimator [63] is based on the weighted field [59]:

$$F(\mathbf{r}) = n_d(\mathbf{r}) - \alpha n_r(\mathbf{r}). \quad (3.4)$$

where \mathbf{r} is the 3D Cartesian coordinate, n_d and n_r are the binned w_{tot} -weighted data and w_{tot} -weighted random catalogues on a grid of cell size $6 h^{-1}$ Mpc, and $\alpha = \sum_{i=1}^{N_d} w_{\text{tot},i(d)} / \sum_{i=1}^{N_r} w_{\text{tot},i(r)}$ rescales the mean density of the random catalogue to the mean data density. The power spectrum multipoles $P_\ell(k)$ can be written as

$$P_\ell(k) = \frac{2\ell + 1}{AN_k} \sum_{\mathbf{k}} F_0(\mathbf{k}) F_\ell(-\mathbf{k}) - \mathcal{SN}_\ell \quad (3.5)$$

where \mathbf{k} is the wavenumber between galaxy pairs and N_k the number of modes in a \mathbf{k} bin, and

$$F_\ell(\mathbf{k}) = \sum_{\mathbf{r}} F(\mathbf{r}) \mathcal{L}_\ell(\hat{\mathbf{k}} \cdot \hat{\mathbf{r}}) e^{i\mathbf{k} \cdot \mathbf{r}}. \quad (3.6)$$

where $\hat{\mathbf{k}} \cdot \hat{\mathbf{r}}$ is the cosine of the angle between the wavenumber vector \mathbf{k} and the line-of-sight $\hat{\mathbf{r}}$. The shot-noise \mathcal{SN}_ℓ is non-zero for $\ell = 0$ as

$$\mathcal{SN}_0 = \frac{1}{A} \left[\sum_{i=1}^{N_d} w_{\text{tot},i(d)}^2 + \alpha^2 \sum_{i=1}^{N_r} w_{\text{tot},i(r)}^2 \right]. \quad (3.7)$$

The normalization term $A = \alpha/dV \sum^k n_{d,k} n_{r,k}$ is summed over a cell with $dV^{1/3} = 10 h^{-1}$ Mpc in size. We compute our observed $P_\ell(k)$ with `PYPOWER`⁸ [64] from 0–0.4 h Mpc $^{-1}$ with $\Delta k = 0.005$ for $\ell = 0, 2, 4$. The χ^2 calculations include $k \in [0.02, 0.35] h$ Mpc $^{-1}$ (Section 3.2).

3.2 Quantifying the Clustering Differences

We use χ_{sys}^2 to describe the differences between the standard clustering and the clustering for mocks with spectroscopic systematics, defined as

$$\chi_{\text{sys}}^2 = (\mathbf{F}_{\ell,\text{std}} - \mathbf{F}_{\ell,\text{sys}})^T \mathbf{C}^{-1} (\mathbf{F}_{\ell,\text{std}} - \mathbf{F}_{\ell,\text{sys}}), \quad (3.8)$$

where \mathbf{F} denotes the vector composed of the two-point statistics multipoles. We calculate the χ_{sys}^2 values for $\mathbf{F}_{\ell=0,2,4} = (\xi_0, \xi_2, \xi_4)$ at $30 < s < 200 h^{-1}$ Mpc in the configuration space and $\mathbf{F}_{\ell=0,2,4} = (P_0, P_2, P_4)$ at $0.02 < z < 0.35 h$ Mpc $^{-1}$ in Fourier space. $\mathbf{F}_{\ell,\text{std}}$ represents the standard clustering measurement which is 1) ELGs from LSS catalogues with w_{tot} (Table 1 from Section 4) and 2) `ABACUSSUMMIT` ELG mocks without catastrophics (Table 2 from Section 5). $\mathbf{F}_{\ell,\text{sys}}$, correspondingly, is the clustering of 1) ELGs with other redshift success corrections and 2) `ABACUSSUMMIT` ELG mocks with different catastrophics. \mathbf{C}^{-1} is the inverse of the analytical covariance matrices. $\sqrt{\chi_{\text{sys}}^2}$ estimates the maximum deviations the systematics can introduce to cosmological measurement rescaled by the cosmic variance. We think the effect of a type of systematics is negligible if $\sqrt{\chi_{\text{sys}}^2} < 1$ (i.e., cosmological impacts $< 1\sigma$). To avoid confusion, we use ε_ξ and ε_P for the 1σ error of the galaxy clustering in the configuration space and Fourier space, respectively in the following sections. They are the square root of the diagonal terms of the analytical covariance matrices $\varepsilon_i = \sqrt{C_{i,i}}$.

⁷<https://github.com/cosmodesi/pycorr>

⁸<https://github.com/cosmodesi/pypower>

3.3 RSD Tests: ShapeFit and Full Modelling

We study the influence of ELG spectroscopic systematics on RSD measurements with full modelling method and ShapeFit compression [65–68]. The full modelling of RSD is to generate model-dependent theoretical power spectra P_{theory} with linear power spectra P_{lin} provided directly by Boltzmann codes such as CLASS [69] and CAMB [70]. This algorithm is thus computationally expensive, since each sampling of cosmology requires the calculation of the accurate P_{lin} . ShapeFit compression, in contrast, is a more efficient, model-independent way of producing P_{theory} from P'_{lin} . The P'_{lin} of ShapeFit is parameterized as follows [71]

$$P'_{\text{lin}}(k) = P_{\text{lin}}^{\text{fid}}(k) \exp \left\{ \frac{m}{a} \tanh \left[a \ln \left(\frac{k}{k_p} \right) \right] \right\}, \quad (3.9)$$

where $P_{\text{lin}}^{\text{fid}}$ is the linear power spectra under the DESI fiducial cosmology, $k_p = \pi/r_d$ is the pivot scale and r_d is the sound horizon scale, $a = 0.6$. m is the free parameter to approximate the accurate linear power spectra. In our tests, we use `VELOCILEPTORS`⁹ for both tests wrapped in `DESILIKE`¹⁰, the DESI cosmological pipeline. To speedup the fitting, we employ the emulator in `DESILIKE` based on the Taylor expansion. The cosmological parameters for full modelling are $\Theta = \{h, \omega_{\text{cdm}}, \omega_b, \log(10^{10} A_s)\}$ where $\omega_* = \Omega_* h^2$. For ShapeFit $\Theta = \{q_{\text{iso}}, q_{\text{AP}}, df, dm\}$, representing the isotropic and anisotropic BAO dilation (see [28] for detailed explanations), $df = f/f^{\text{fid}}$ is the difference between the measured linear growth rate f and the fiducial value, $dm = m - 1$.

To take into account the observational geometry, we need to apply the window matrix $W_{\tilde{\ell}, \ell}$ on $P_{\ell, \text{theory}}$ as $\tilde{P}_{\tilde{\ell}, \text{theory}}(\tilde{k}_i) = \sum_j W_{\tilde{\ell}, \ell}(\tilde{k}_i, k_j) P_{\ell, \text{theory}}(k_j)$. Assuming a Gaussian likelihood $L(\Theta) = \exp(-\chi^2(\Theta)/2)$, where χ^2 is defined as

$$\chi^2 = (\mathbf{P}_{\ell, \text{mock}} - \tilde{\mathbf{P}}_{\tilde{\ell}, \text{theory}})^T \mathbf{C}^{-1} (\mathbf{P}_{\ell, \text{mock}} - \tilde{\mathbf{P}}_{\tilde{\ell}, \text{theory}}), \quad (3.10)$$

$\mathbf{P}_{\ell=0,2} = (P_0, P_2)$ represent the data vector of systematics-uncontaminated and contaminated mocks, $\tilde{\mathbf{P}}_{\ell=0,2} = (\tilde{P}_0, \tilde{P}_2)$ is the data vector of geometry-modulated theory. We consider $0.02 < k < 0.2 h \text{ Mpc}^{-1}$ in the RSD fitting.

4 Redshift Success Rate Corrections

4.1 The Redshift Failure Weight w_{zfail}

Redshift failures are observed objects that do not have reliable redshift measurements. They are dropped from the LSS catalogue and thus may lead to an underestimation of galaxy density in the observed 3D map of the Universe. A straightforward way of making up for the absence of objects is to up-weight the nearest object to the failed observation on the sky, i.e., count it as two objects when calculating the galaxy clustering. This simple weighting scheme was used in LRGs from the Baryon Oscillation Spectroscopic Survey (BOSS, 2008–2014; [72]) from SDSS-III [73]. It worked well as the failed redshift measurements were distributed randomly on the focal plane and only composed of less than 2% of the total observation [74].

However, when the failure rate rises to 10% or higher, as seen with LRGs from the extended Baryon Oscillation Spectroscopic Survey (eBOSS, 2014–2020; [75]) of SDSS-IV [76] and ELGs from eBOSS and DESI [5, 17], such a simple up-weighting approach becomes ineffective. This is because it assumes that the properties of galaxies with failed redshifts are similar to those of the successful

⁹<https://github.com/sfschen/velocileptors>

¹⁰<https://github.com/cosmodesi/desilike>

samples, which is often too strong (see [17] for the example of ELGs). In such cases, the goal of correcting failed redshift measurements should be to restore the uniformity of the redshift success rate across varying observing conditions rather than striving for a 100% success rate. Similar to [77], we model the observed redshift success rate f_{goodz} as a function of observing conditions and use it to construct the w_{zfail} weight. To simplify the $f_{\text{goodz}}^{\text{m}}$, we normalize the f_{goodz} as shown in Eq. (2.3).

The primary observing condition influencing f_{goodz} is the observational squared SNR of ELG spectra TSNR2_ELG ($S_{\text{spec,obs}}$ hereafter), which is proportional to the effective observing time. $S_{\text{spec,obs}}$ is defined as follows [36]

$$S_{\text{spec,obs}} = \sum_i T_i^2 \langle (\delta F)^2 \rangle_i \sigma_i^{-2}, \quad (4.1)$$

where T is the calibration coefficient of photon-electron conversion measured from each observed spectrum, involving the product of throughput¹¹ (the system's efficiency of collecting incoming photons) and the real exposure time. $\langle (\delta F)^2 \rangle$ is the squared spectral line flux averaged over all spectral templates. σ^2 is the noise variance, including the instrumental noise and sky spectra. i is the wavelength index of the whole spectrum. All else held constant, f_{goodz} should be monotonic with $S_{\text{spec,obs}}$.

In addition to $S_{\text{spec,obs}}$, we find that f_{goodz} also varies as the redshift. This is because the sky emission lines appear at distinct wavelengths corresponding to distinct redshifts at which [O II] emission can be observed (see Section 7.2 of [17] for example). The f_{goodz} at these redshifts are lower than the others because the noise level (the flux of sky-spectrum residuals) is high for [O II] detections.

We aim to obtain a redshift failure weight w_{zfail} that corrects the f_{goodz} dependences on $S_{\text{spec,obs}}$ and redshift. This correction is part of the total weight w_{tot} in DR1 ELG LSS catalogue as introduced in Section 2.1. But w_{zfail} is constructed for all observed ELG targets, including those without reliable redshift measurements. Bearing this in mind, it is necessary to find quantities other than the 'redshift' itself to embody the challenges of [O II] detection in the presence of sky emission lines.

4.1.1 [O II] Emission and Redshift Measurement

First, we compute the median [O II] flux ratio as a function of redshift, i.e., $[\text{O II}]_R(z)$. It is an empirical measure of how difficult it is to obtain a successful ELG redshift measurement as a function of redshift, thus critical in modelling f_{goodz} . We define it as

$$[\text{O II}]_R(z) = \frac{\overline{F}_{[\text{O II}]}(z) \Big|_{S_{\text{spec,obs}} < \overline{T}_{\text{ELG}}}}{\overline{F}_{[\text{O II}]}(z) \Big|_{S_{\text{spec,obs}} > \overline{T}_{\text{ELG}}}}, \quad (4.2)$$

where $\overline{F}_{[\text{O II}]}$ is the median [O II] flux of ELGs with reliable redshift measurements (samples from N_{goodz} in Eq. (2.3)). $\overline{T}_{\text{ELG}} \approx 123$ is the median $S_{\text{spec,obs}}$ of ELGs with appropriate observing conditions (samples from N_{obs} in Eq. (2.3)). $[\text{O II}]_R(z)$ is relevant, as the dominant factor in the redshift success criteria Eq. (2.2) is the SNR of the observed [O II] flux. The object must have a larger [O II] flux to secure a good redshift measurement when the spectrum is noisier. We, therefore, observe a larger $[\text{O II}]_R(z)$ at $z > 1.5$ due to the interference of the sky emission lines to [O II] measurements at that redshift range on the left panel of Figure 1. In DESI DR1, we assume that [O II] emitters with higher [O II] flux are the same population as those with lower [O II] flux, i.e., their clustering is consistent (e.g., see [78] for example). $[\text{O II}]_R(z)$ is calculated at $z \in [0.8, 1.6]$, the clustering measurement range, with $dz = 0.01$ to have a balance between true features and noise.

¹¹Figure 27 of [11] present the throughput of DESI instrument.

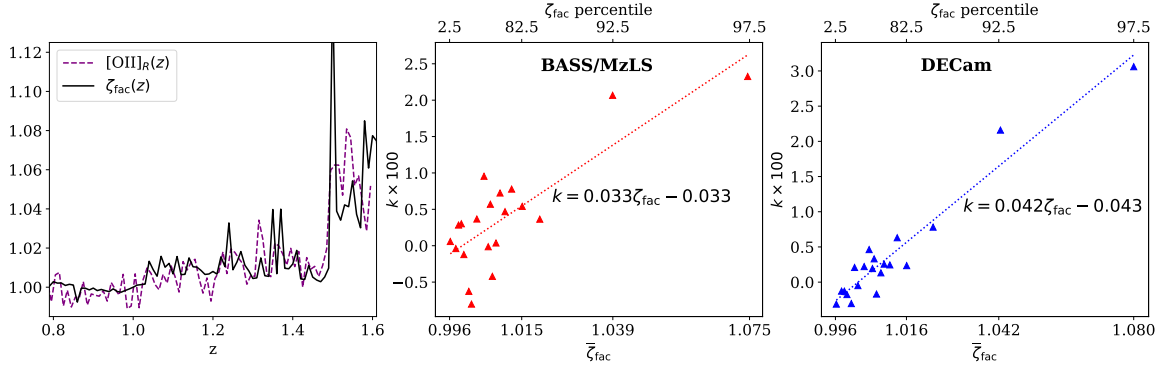


Figure 1. *Left:* $[\text{O II}]_R$ (the dashed line) and ζ_{fac} (the solid line) as a function of the redshift. $\zeta_{\text{fac}}(z)$ (from spectra template) is a good representation of the observed $[\text{O II}]_R(z)$, describing the difficulty (the larger they are, the more difficult) of obtaining a good redshift measurement. *Middle:* The 20 slopes k and their corresponding $\bar{\zeta}_{\text{fac}}$ (the bottom x-label) and ζ_{fac} percentiles (the top x-label) for BASS/MzLS. We implement linear regression on the k - $\bar{\zeta}_{\text{fac}}$ relation and the best-fit relation is shown in the dotted line and the text. *Right:* the same as the middle panel but for DECam data.

Next, we need to find a theoretical curve that embodies the characteristics of $[\text{O II}]_R(z)$ at $z \in [0.8, 1.6]$ to build f_{goodz}^m . The theoretical squared SNR of ELG spectra $S_{\text{spec,theo}}(z)$ plays a role here, defined as

$$S_{\text{spec,theo}}(z) = \sum_i F_{e,i}^2(z) \sigma_{F,i}^{-2}, \quad (4.3)$$

where $F_e(z)$ is the flux of emission lines¹² at redshift z averaged over 50 processed ELG templates. These template spectra get their continuum removed, and their emission lines are shifted to the wavelength corresponding to redshift z for $F_e(z)$ calculation. σ_F^{-2} is the inverse variance of the sky spectra obtained in a standard exposure and averaged over the 10 DESI spectrographs¹³. i is the wavelength index, and thus, the sum is performed over all DESI wavelength for $\lambda \in [3600, 9800] \text{ \AA}$. Thus, this quantity estimates how an ELG target's cumulative squared SNR should change with its redshift z . Numerically, we compute $S_{\text{spec,theo}}(z)$ with a redshift resolution of $dz = 0.001$ at redshift $z \in [0, 1.6]$ to embody the influence of sky-residual spikes on the redshift measurement.

We find that a simple transformation of $S_{\text{spec,theo}}(z)$ as follows:

$$\zeta_{\text{fac}}(z) = \begin{cases} 1 + \frac{1500/S_{\text{spec,theo}}(z) - 1}{15/(z-1)}, & 0 < z < 1.6 \\ 1, & \text{otherwise} \end{cases}, \quad (4.4)$$

match both the general and fine features in $[\text{O II}]_R(z)$ as shown in the left panel of Figure 1 despite small deviations. In this way, we assign a ζ_{fac} value to all ELGs with successful redshifts to represent the difficulty of obtaining such a good redshift measurement.

4.1.2 The f_{goodz} Model and w_{zfail} Weight

Now we have $\zeta_{\text{fac}}(z)$ and $S_{\text{spec,obs}}$ for every ELG with proper observing conditions and we expect our f_{goodz}^m to increase with these two quantities monotonically. In practice, we split these ELGs in 20 bins of ζ_{fac} , each with the same number of galaxies. In each ζ_{fac} bin i , we fit a linear relationship

¹²This not only includes $[\text{O II}]$ doublets, but also other lines such as $[\text{O III}]$, $\text{H}\beta$.

¹³Specifically, we use exposure 165078 observed on January 28th, 2023.

$k_i S_{\text{spec,obs}} + b_i$ to $f_{\text{goodz},i}$ in 10 evenly spaced bins of $80 < S_{\text{spec,obs}} < 200$. All fits assume Poissonian errors for $f_{\text{goodz},i}$, i.e., $\epsilon_f = \sqrt{N_{\text{goodz}}/N_{\text{obs}}}$.

We then take the 20 slopes k_i and their corresponding median $\bar{\zeta}_{\text{fac},i}$ and perform a least-squares linear fit (errors are assumed to be the same given the number of galaxies was the same for each k_i calculation) to obtain

$$k = C_1 \zeta_{\text{fac}} + C_0. \quad (4.5)$$

This process is repeated separately for the BASS/MzLS and DECam regions, and the results, including the best-fit lines and parameters, are shown in the middle and right panel of Figure 1. Note that the largest 90% ζ_{fac} , though having significantly larger k_i , agrees with the k - ζ_{fac} trend of the smaller ζ_{fac} . Therefore, we do not implement more complicated regression and stability checks of these two k - ζ_{fac} relations in this study. We will discuss the consequence of this choice in Section 4.3.

Finally, we convert the parameterized slope to a weight that can be attached to the galaxy catalogues to remove any trends between f_{goodz} and $(S_{\text{spec,obs}}, z)$. We expect the redshift success should only increase as a function of $S_{\text{spec,obs}}$. Thus, we clip k such that it has a minimum value of 0:

$$k(\zeta_{\text{fac}}) = \begin{cases} C_1 \zeta_{\text{fac}} + C_0, & k > 0 \\ 0, & \text{otherwise.} \end{cases} \quad (4.6)$$

Assuming the intercept $b = 1 - k\bar{T}_{\text{ELG}}$, with \bar{T}_{ELG} being the median $S_{\text{spec,obs}}$ of all ELG targets with appropriate observing conditions, we now have a f_{goodz}^m as a function of redshift z and $S_{\text{spec,obs}}$

$$f_{\text{goodz}}^m(S_{\text{spec,obs}}, z) = k(\zeta_{\text{fac}}[z])(S_{\text{spec,obs}} - \bar{T}_{\text{ELG}}) + 1. \quad (4.7)$$

We simply use the inverse of this for the weight to attach to the galaxy catalog

$$w_{\text{zfail}}(S_{\text{spec,obs}}, z) = 1/f_{\text{goodz}}^m(S_{\text{spec,obs}}, z). \quad (4.8)$$

Figure 2 presents the $f_{\text{goodz}}-S_{\text{spec,obs}}$ relation before and after w_{zfail} correction for samples from BASS/MzLS and DECam surveys. ELGs with good redshifts are split into finer bins with $dz = 0.1$ at $0.8 < z < 1.6$ for f_{goodz} computation. The errors are binomial errors ϵ_{zfail}

$$\epsilon_{\text{zfail}} = \frac{\sqrt{N_{\text{obs}}(1 - N_{\text{goodz}}/N_{\text{obs}})}}{N_{\text{obs}}} \quad (4.9)$$

and their $\chi_{\text{zfail}}^2 = (f_{\text{goodz}} - 1)^2/\epsilon_{\text{zfail}}^2$ represents the deviation from a uniform $f_{\text{goodz}}-S_{\text{spec,obs}}$ relation. The mean values of f_{goodz} fluctuate a bit, but all relations are consistent with monotonic tendencies. The $f_{\text{goodz}}-S_{\text{spec,obs}}$ dependency in both footprints is close to unity before the w_{zfail} correction, except for the $\sim 10\%$ -level variations at $1.3 < z < 1.4$ and the $\sim 30\%$ -trend at $1.5 < z < 1.6$. They correspond to the big spikes of $[\text{O II}]_R(z)$ and ζ_{fac} in the left panel of Figure 1. Therefore, w_{zfail} based on ζ_{fac} suppress the dependences of f_{goodz} on $S_{\text{spec,obs}}$ at $1.2 < z < 1.6$, especially on $1.5 < z < 1.6$ given the decreasing χ_{zfail}^2 . Note that the $\chi_{\text{zfail}}^2/\text{dof}$ values can still be as large as 3. But we do not worry about it as they represent a sub-percent f_{goodz} difference, leading to a minor impact on the clustering as presented in Section 4.3.

4.2 The Focal Plane Correction η_{zfail}

The f_{goodz} not only depends on $(S_{\text{spec,obs}}, z)$. It also varies across the focal plane (e.g., [5]). But $S_{\text{spec,obs}}$ is defined for each exposure, without information on the focal plane. The definition of ζ_{fac} used

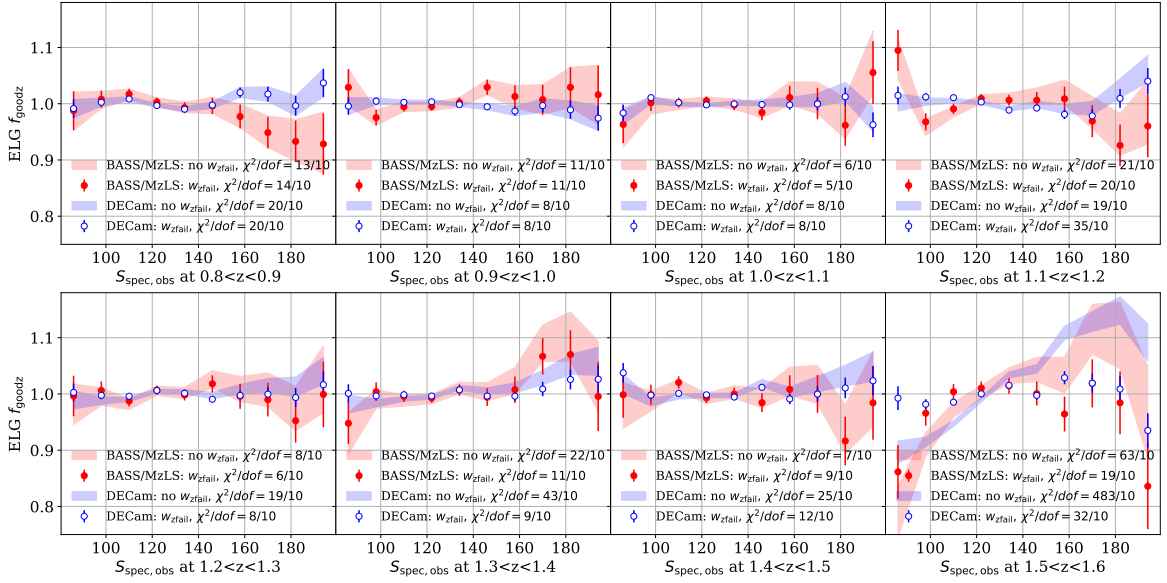


Figure 2. The $f_{\text{goodz}}-S_{\text{spec,obs}}$ relation before (shades) and after (error bars with dots) w_{zfail} correction in fine redshift bins at $0.8 < z < 1.6$ with $dz = 0.1$. BASS/MzLS and DECam results are presented in red/closed circles and blue/open circles, respectively. w_{zfail} removes f_{goodz} dependences on $S_{\text{spec,obs}}$ at $z > 1.2$, especially at $1.5 < z < 1.6$, where the sky emissions are big issues for ELGs by construction.

quantities that are averaged over spectrographs, eliminating the information as well. Consequently, w_{zfail} does not remove the f_{goodz} variations on the focal plane as shown in Figure 3. The left and middle panel shows a 10% f_{goodz} variation across the focal plane, resulting in $\chi^2_{\text{zfail}}/\text{dof} = 4753/4262$ for BASS/MzLS and $\chi^2_{\text{zfail}}/\text{dof} = 4716/4262$ for DECam where 4262 is the number of fibres. Note that the median number of good redshift measurements per fibre for BASS/MzLS survey is 101, and that for DECam is 575. The smaller statistics of BASS/MzLS lead to larger f_{goodz} variations and error bars, thus similar χ^2_{zfail} to DECam. Marginalising over the angular direction, the f_{goodz} of fibres that are close to the focal centre shows 1% higher f_{goodz} than that of the distant fibres as shown in the right panel of Figure 3. This difference still exists with w_{zfail} corrections despite the fact that it is already close to the ideal case of a uniform distribution. Therefore, we need an extra w_{zfail} correction factor on w_{zfail} as a function of its position on the focal plane (or a fibre-dependent correction).

The correction of w_{zfail} is defined fiber-wise as:

$$\eta_{\text{zfail},i} = \bar{f}_{\text{goodz}}(i) / f_{\text{goodz}}(i), \quad (4.10)$$

where i is the fibre ID ranging from 0 to 4999, but only 4262 of them provide f_{goodz} measurements. The other 738 fibres are not used for scientific observations¹⁴. $f_{\text{goodz}}(i)$ is the f_{goodz} of fibre i and $\bar{f}_{\text{goodz}}(i)$ is the mean f_{goodz} of all samples. η_{zfail} null all f_{goodz} on the focal plane by definition, and thus, the f_{goodz} dependence on the distance to the focal centre is removed in both the BASS/MzLS and DECam footprints. This fibre-wise correction is then implemented on each observed ELG target, and thus, the new total weight w'_{tot} is written as

$$w'_{\text{tot}} = w_{\text{comp}} w_{\text{sys}} (w_{\text{zfail}} \eta_{\text{zfail}}), \quad (4.11)$$

where $w_{\text{zfail}} \eta_{\text{zfail}}$ is the corrected redshift failure weight.

¹⁴They mostly are stuck fibres, but we can still use them to obtain sky spectra

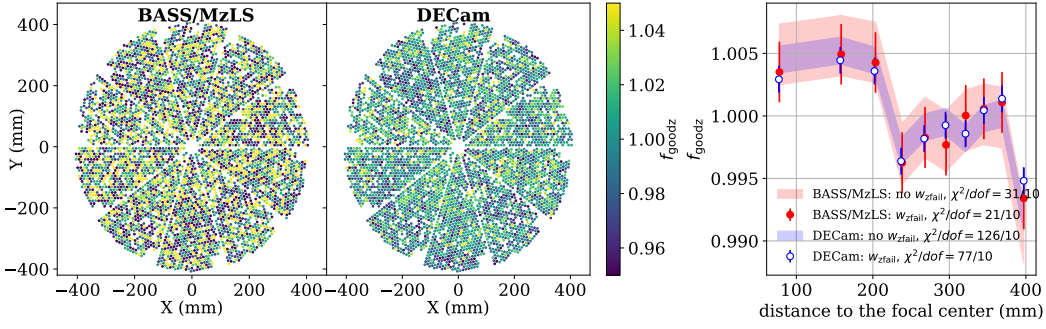


Figure 3. *Left:* The f_{goodz} (with w_{zfail}) of each fibre distributed on the focal plane for BASS/MzLS survey. The f_{goodz} differences on the focal plane can be as large as 10%. *Middle:* the same as the left panel but for DECam survey. Its f_{goodz} variations are smaller than that of BASS/MzLS survey. *Right:* f_{goodz} as a function of the distance to the focal centre without (shades) and with (error bars) w_{zfail} corrections. Red/closed circles and blue/open circles represents results from BASS/MzLS and DECam respectively. The f_{goodz} variations on the focal plane are independent of $(S_{\text{spec,obs}}, z)$, thus w_{zfail} does not eliminate this dependence.

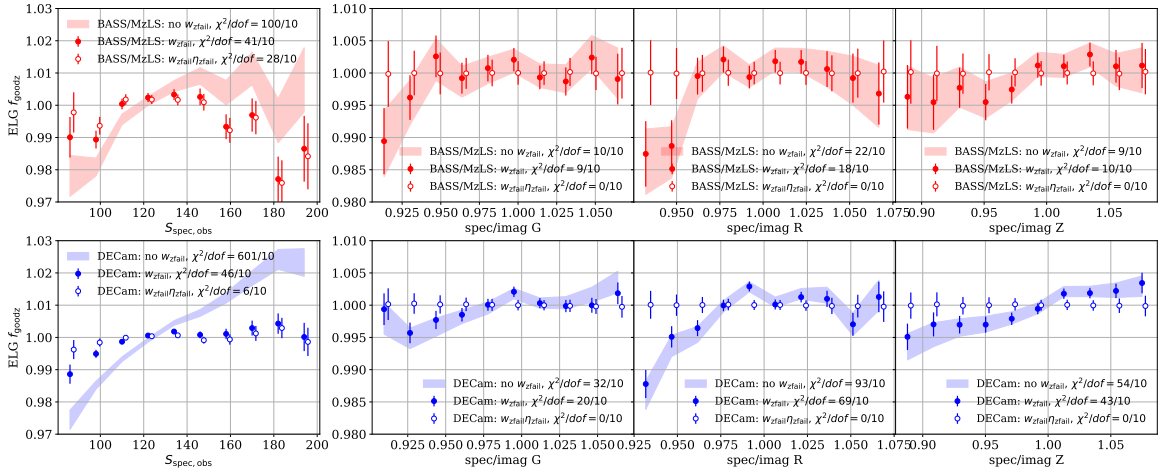


Figure 4. The f_{goodz} dependencies on $S_{\text{spec,obs}}$ (the first column) and on averaged ratios of spectroscopic and imaging flux of standard stars in G (the second column), R (the third column) and Z (the fourth column) bands without w_{zfail} (lines with shades), with w_{zfail} (closed error bars) and with $w_{\text{zfail}}\eta_{\text{zfail}}$ (open error bars) for BASS/MzLS regions (the upper panel) and DECam regions (the lower panel). The remaining f_{goodz} trends not corrected by w_{zfail} were removed by $w_{\text{zfail}}\eta_{\text{zfail}}$.

4.3 Performances of w_{zfail} and η_{zfail}

We have proved in Section 4.1 and Section 4.2 that w_{zfail} and η_{zfail} can respectively correct the f_{goodz} dependences on $S_{\text{spec,obs}}$ in fine redshift bins and the focal plane by construction. In this section, we will check their performance of removing other f_{goodz} trends and their influences on galaxy clustering.

In the first column of Figure 4, the dependence of f_{goodz} on $S_{\text{spec,obs}}$ for ELGs targets without redshift selection is around 5% (shades) and w_{zfail} suppresses the trend down to 1% (closed error bars). The improvements are also significant, as shown in the decreasing χ^2_{zfail} values in both BASS/MzLS and DECam regions. Therefore, w_{zfail} is included in the ELG LSS catalogue as part of the correction of observational systematics (Eq. (2.1)). The over-suppression of BASS/MzLS f_{goodz} for those with large $S_{\text{spec,obs}}$ ($\sim S_{\text{spec,theo}}$) probably come from the imperfect linear regression on small ζ_{fac} values as shown in the middle panel of Figure 1. The open circles in the same subplots illustrate the effects

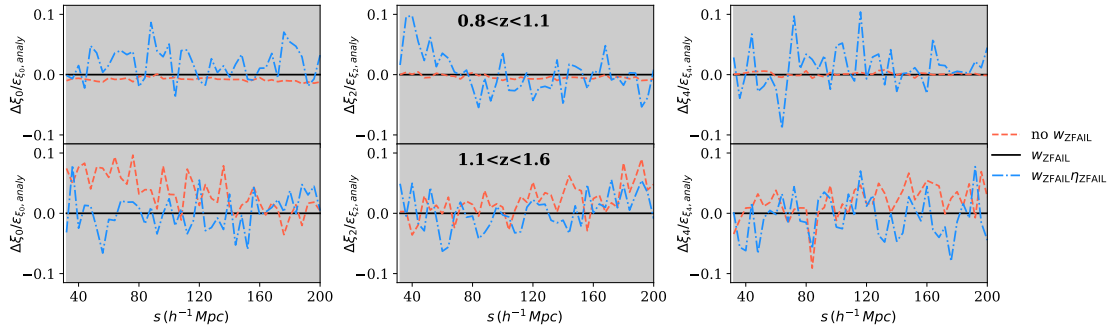


Figure 5. The comparison of 2PCF monopole (first column), quadrupole (second column) and hexadecapole (third column) for ELGs implementing the standard weighting scheme w_{tot} (w_{zfail} , solid lines), the w_{tot} but excluding w_{zfail} ($\text{no } w_{\text{zfail}}$, dashed lines) and the new total weight w'_{tot} ($w_{\text{zfail}}\eta_{\text{zfail}}$, dash-dotted lines) at $20 < s < 200 h^{-1} \text{ Mpc}$. The first row is for ELGs at $0.8 < z < 1.1$, and the second is for $1.1 < z < 1.6$. The clustering influences of redshift failure weights are minor, with a difference of $< 0.05\epsilon_{\xi}$.

of $\eta_{\text{zfail}}w_{\text{zfail}}$ on the same f_{goodz} trends as in Figure 4. This extra correction brings back missing information on the focal plane by w_{zfail} and, therefore, improves f_{goodz} weighting in small $S_{\text{spec,obs}}$. This agrees with our conclusion that the source of the over-correction of f_{goodz} in BASS/MzLS area is from the w_{zfail} modelling, not from any uncorrected f_{goodz} trend on the focal plane. We also notice that ζ_{fac} is not a perfect representation of $[\text{O II}]_R(z)$. We will develop a better f_{goodz}^m for future data release as these aspects a minor effect on the clustering.

The second to fourth panels of Figure 4 illustrates the f_{goodz} dependence on the spectrograph-to-imaging flux ratio of standard stars at $\lambda \in [4500, 5500] \text{ \AA}$ (G band), $\lambda \in [6000, 7300] \text{ \AA}$ (R band) and $\lambda \in [8500, 9800] \text{ \AA}$ (Z band). They represent the fibre aperture loss in the central wavelength of these three bands [36]. As the definition of $S_{\text{spec,obs}}$ includes the throughput of the fibre (Eq. (4.1)), we expect that f_{goodz} varies with throughputs, and w_{zfail} can also remove most of the f_{goodz} dependences on throughputs. The fibre aperture loss in R and Z bands present a more significant trend than in G band as the $[\text{O II}]$ emissions of DESI ELG targets are observed in R and Z bands. But the f_{goodz} dependences on the throughputs remain after applying w_{zfail} as shown in Figure 4. This is consistent with our finding in Figure 3 that w_{zfail} by construction does not include the modelling of f_{goodz} variations on the focal plane. The new weight, $\eta_{\text{zfail}}w_{\text{zfail}}$, nullifies the f_{goodz} dependences on the throughputs by construction. This is because η_{zfail} , defined per-fibre, eliminates the 2D f_{goodz} variations on the focal plane. Consequently, any quantities defined based on fibres will have a unity mean f_{goodz} after applying η_{zfail} . However, such an *ad hoc* correction might have the risk of overfitting the DR1, so it is not part of the LSS weight budget. We may consider adding it to w_{tot} in the future data release.

We then study the effects of w_{zfail} and $w_{\text{zfail}}\eta_{\text{zfail}}$ on galaxy clustering. To do this, we calculate the 2PCF $\xi_{\ell}(s)$ and power spectra $P_{\ell}(k)$ of ELGs from the LSS catalogues at $0.8 < z < 1.1$ and $1.1 < z < 1.6$ (redshift bins for LSS analyses). The galaxy weight of ELGs is the product of w_{FKP} and the total observational weight in three formats: w_{tot} (Eq. (2.1)), $w_{\text{tot}}/w_{\text{zfail}}$ (no corrections on the failed redshift measurements) and w'_{tot} (Eq. (4.11), the complete LSS weights with the new redshift failure weight). They are denoted as w_{zfail} , $\text{no } w_{\text{zfail}}$ and $w_{\text{zfail}}\eta_{\text{zfail}}$ respectively in Figure 5 and Figure 6. These two figures present the clustering effects of the redshift failure weights compared to the standard w_{tot} weight in the configuration space and Fourier space. Both weights have $< 0.05\epsilon$ influence on all two-point statistics multipoles at both redshift bins (see Section 3.2 for the definition of the $1\text{-}\sigma$ clustering error ϵ). Such a minor effect of the redshift failure weights has been observed

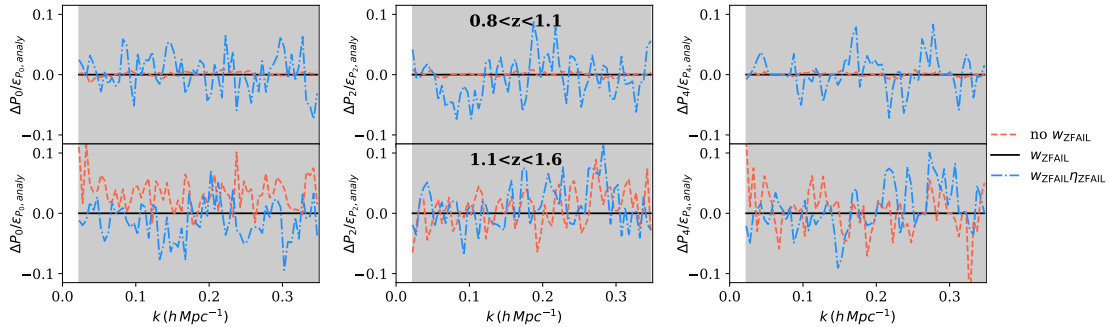


Figure 6. Similar to Figure 5 but for power spectra multipoles $P_\ell(k)$ at $0.02 < k < 0.35 \text{ h Mpc}^{-1}$. The clustering influences of redshift failure weights in the Fourier space are as small as those in the configuration space.

Space	redshift	$\chi_{\text{sys, no } w_{\text{zfail}}}^2$	$\chi_{\text{sys, } w_{\text{zfail}} \eta_{\text{zfail}}}^2$
Config.	$0.8 < z < 1.1$	0	0.2
	$1.1 < z < 1.6$	0.15	0.18
Fourier	$0.8 < z < 1.1$	0	0.22
	$1.1 < z < 1.6$	0.32	0.25

Table 1. The χ_{sys}^2 values for the ELG clustering calculated with different weights compared to the standard clustering with the w_{tot} weight in both configuration space and Fourier space for $\ell = 0, 2, 4$. The third column shows ELGs implementing w_{tot} but excluding w_{zfail} , and the fourth column is for ELGs applying w'_{tot} (Eq. (4.11)), which includes the corrected failure weight $w_{\text{zfail}} \eta_{\text{zfail}}$. In both configuration and Fourier spaces, the influences of the redshift failure weight and its correction are minor regardless of the redshift range.

in eBOSS ELGs as well [5]. w_{zfail} leads to a larger clustering impact at $1.1 < z < 1.6$ compared to the clustering at $0.8 < z < 1.1$. This is implied in Figure 2 as the significant corrections that w_{zfail} accomplished are all at $1.1 < z < 1.6$. The effect of $w_{\text{zfail}} \eta_{\text{zfail}}$ on redshift ranges and multipoles are all comparable, showing the impact of the 2D η_{zfail} correction is evenly applied to all samples.

Table 1 provides the χ_{sys}^2 values of ELG clustering computed without w_{zfail} and with the new total weight w'_{tot} (Eq. (4.11)) compared to the standard clustering computed with w_{tot} . These values are no larger than 0.32. So, we conclude that the cosmological impact of w_{zfail} and its correction η_{zfail} can be neglected. Nevertheless, it is important to note that f_{goodz} not only depends on the effective exposure time $S_{\text{spec,obs}}$ and redshift z . f_{goodz} of each fibre also varies on the focal plane, independent of the variations brought by $(S_{\text{spec,obs}}, z)$. Therefore, future surveys must check the dependence of f_{goodz} on different observing conditions and their correlation to develop a complete weight to correct the failed redshift measurements.

5 Redshift Catastrophics and Redshift Uncertainty

Catastrophics and redshift uncertainty are systematics hidden in ELG samples with secure redshift measurements (Eq. (2.2)). With $\Delta v = \Delta z c / (1 + z)$ from repeated observations (Section 2.1.2), the catastrophics refer to pairs of redshift with a large $|\Delta v|$. There are several definitions of ‘a large $|\Delta v|$ ’, which are $|\Delta v| > 1000 \text{ km s}^{-1}$ [17, 75] (our definition), $\Delta v > 5\sqrt{\langle \Delta v^2 \rangle}$ [79], or those with clear evidence of misidentification of emission lines or between the emission line and the sky residuals

[3]. All these definitions mean that the radial position of a small number of tracers is shifted to a large extent, leading to imprints on the clustering. ELGs from DESI EDR and SDSS-IV eBOSS have $f_{\text{catas}} \sim 0.3\%$ [5, 17]. Given such a small fraction, its clustering and cosmological impacts are neglected in eBOSS analyses.

Redshift uncertainty comes from redshift measurement and thus exists in every galaxy in LSS catalogues. Repeated observations without the catastrophics samples provide a statistical estimation via the width of the Δv distribution (e.g. [17, 80, 81] from SDSS-IV eBOSS). Note that repeated observations cannot capture the velocity shift of QSOs, which is part of QSO redshift uncertainty. But we can study this type of mixed uncertainty via their clustering effects (see [53, 82]). For galaxy samples, we assume statistical uncertainty represents the redshift uncertainty. The redshift uncertainty of DESI ELGs from EDR is $\sim 8 \text{ km s}^{-1}$, leading to little impact on the clustering [17, 53].

Given their properties, neither catastrophics nor redshift uncertainty can be corrected target-wise like $w_{z\text{fail}}$ but they influence the clustering collectively. Catastrophics of line emitters (i.e., ELGs) are poorly understood due to the limited statistics and small fraction as mentioned above. Now, with millions of reliable ELG samples from DESI DR1 [14] and well-modelled, realistic ELG mocks [55], we have enough good-quality samples to study the effect of catastrophics carefully. DESI DR1 have fewer samples with long exposure compared to EDR [12] to guarantee better redshift measurements. Therefore, we will revisit these two aspects in DESI DR1 ELGs, understand the data, model them with galaxy mocks, and see how to prevent them from biasing the cosmological measurements.

5.1 Characterising the Catastrophics

Catastrophics are discrepancies in the redshift measurements for the same object. As reported in Section 2.1.2, 0.26% of the repeated ELG pairs have $|\Delta v| > 1000 \text{ km s}^{-1}$. There is no preference for their locations in the focal plane, and their redshift distributions are shown in Figure 7. The upper panel of Figure 7 compares the *true* redshift (z_{true}) and the *catastrophics* redshift (z_{catas}) for the ELG catastrophics detected with the repeated observation catalogue. We determine the z_{true} and z_{catas} via visual inspection of their reduced spectra with the help of `prospect`¹⁵ [52, 83]. If a redshift measurement matches secure spectral features (e.g., the [O II] doublets or multiple emission lines), this redshift is z_{true} and the other measurement on the same object is z_{catas} . There are five types of catastrophics for ELGs shown in Figure 7 (see Appendix A for examples of their spectra):

- The misidentification of the residuals of sky emissions at around 8600–8700 Å to be the [O II] emission (sky confusion hereafter). They form a prominent feature in Figure 7 at $z_{\text{catas}} \approx 1.32$ as shown in crosses, comprising 26.7% of the total catastrophics samples. We observe a significant doublet-like spike in one of their spectra at 8600–8700 Å, which is difficult to smooth out and, therefore, is identified as the [O II] emission. The evolving DESI redshift pipeline might resolve this issue by improving the sky subtraction and line-identification process [36]. There is no such feature in the other spectrum of these repetitively observed objects, and thus, the redshift obtained by the other spectrum is correct (z_{true}).
- The misidentification of the sky residuals at other wavelengths as the [O II] emission. The sky emissions/residuals appear at $\lambda > 8000 \text{ Å}$, corresponding to $z_{\text{catas}} > 1.1$. As the [O II] flux of ELGs at $z_{\text{true}} < 1.1$ is systematically lower than the sky residuals (see Figure 15 of [17]), this type of catastrophics tends to increase the redshift of ELGs, i.e., from $z_{\text{true}} < 1.1$ to $z_{\text{catas}} > 1.1$. They make up 27.6% of the total catastrophic pairs.

¹⁵<https://github.com/biprateep/prospect>

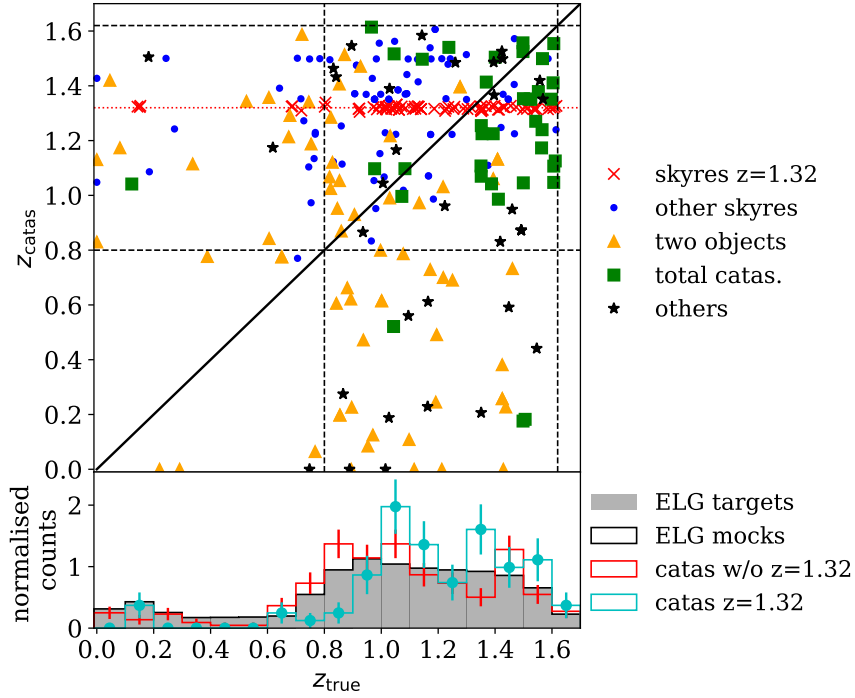


Figure 7. *Top:* The comparison between the *true* redshift and the *catastrophics* redshift for catastrophics of DESI ELGs. The exceptions are spectra that contain two objects (triangles), which means that both redshifts are true redshifts, and spectra that have no emission lines for redshift determination (squares), which means that both redshifts are catastrophically failed redshifts. The cross, small dots represent the redshift misidentification of the sky residuals to be the $[\text{O II}]$ emission that concentrates on $z_{\text{catas}} \approx 1.32$ (the horizontal dotted line), the same misidentification of sky residuals at other wavelengths. Stars are all other types of catastrophics. The dashed lines in $z = 0.8$ and $z = 1.6$ indicate the redshift range of ELGs for clustering measurements. *Bottom:* The (true) redshift distribution of the full catalogue (grey shades), the ELG ABACUSSUMMIT mocks (solid line), the catastrophics without $z_{\text{catas}} \approx 1.32$ (step histogram with error bars only), and the catastrophics with $z_{\text{catas}} \approx 1.32$ (step histogram with dotted error bars). The error bars of both catastrophics samples are assumed to be binomial errors. The redshift distribution of two types of catastrophics roughly follows the full catalogue.

- Two objects in the spectra. The fibre might capture two overlapping objects with different redshifts, or the ELG spectra were contaminated by a bright, nearby object (z_{catas} or z_{true} around 0). As there are two sets of spectral features and thus true redshifts, the redshift pipeline can take either as its output redshift. These samples are mainly at $0.6 < z < 0.9$ and comprise 22.0% of the total catastrophics.
- Total catastrophics. There are 12.1% catastrophics that do not have a correct redshift measurement at all. This is because the $[\text{O II}]$ emission is too faint to be found (by the REDROCK pipeline and visual inspection). Therefore, REDROCK can identify any of sky residuals as $[\text{O II}]$ doublets. Their z_{true} and z_{catas} concentrate at $z > 1.1$ because most of the sky residuals are at $\lambda > 8000 \text{ \AA}$ as mentioned above.
- Other catastrophics. The remaining 11.6% catastrophics include line confusion between $[\text{O II}]$ doublets and other emission lines such as $[\text{O III}]$ and $\text{H}\alpha$, bad spectra, and QSO spectra misclassified as ELGs.

Although there are five patterns of catastrophics, we only need to model the excess sky confusion and all the other patterns (random catastrophics hereafter). The random catastrophics alone cannot reproduce the distinct feature of $z_{\text{catas}} \approx 1.32$. Random catastrophics with additional sky confusions should represent more general catastrophics while avoiding overfitting our specific sample.

The z_{catas} distribution of the sky confusion (left) and the $\log_{10}(|\Delta v|)$ ($\hat{\Delta v}$ hereafter) distribution of random catastrophics (right) are presented in Figure 8. We fit the excess sky confusion with a Gaussian distribution $\mathcal{N}(\mu_{\text{sky}}, \sigma_{\text{sky}}^2)$ where $\mu_{\text{sky}} = 1.32$ and $\sigma_{\text{sky}} = 0.006$, enclosing 24.9% of the total catastrophics. This Gaussian function is shifted up by 0.61, representing the remaining 1.9% sky confusion that has been included in random catastrophics. The $\hat{\Delta v}$ distribution of the random catastrophics can be fitted with a Gaussian profile, a Lorentzian profile and a log-normal profile with an extra free parameter $\mathcal{LN}(\mu_{\text{ran}}, \sigma_{\text{ran}}^2, \hat{v}_0; \hat{\Delta v})$ which is defined as

$$\mathcal{LN}(\mu_{\text{ran}}, \sigma_{\text{ran}}^2, \hat{v}_0; \hat{\Delta v}) = \frac{A}{\sqrt{2\pi}\sigma_{\text{ran}}(-\hat{\Delta v} + \hat{v}_0)} \exp\left\{-\frac{\left[\ln(-\hat{\Delta v} + \hat{v}_0) - \mu_{\text{ran}}\right]^2}{2\sigma_{\text{ran}}^2}\right\}. \quad (5.1)$$

Assuming a binomial error, the log-normal profile provides a much better fitting to the $\hat{\Delta v}$ distribution of random catastrophics. Its best-fitting parameters are $A = 0.99$, $\mu_{\text{ran}} = 0.64$, $\sigma_{\text{ran}} = 0.25$, $\hat{v}_0 = 6.62$.

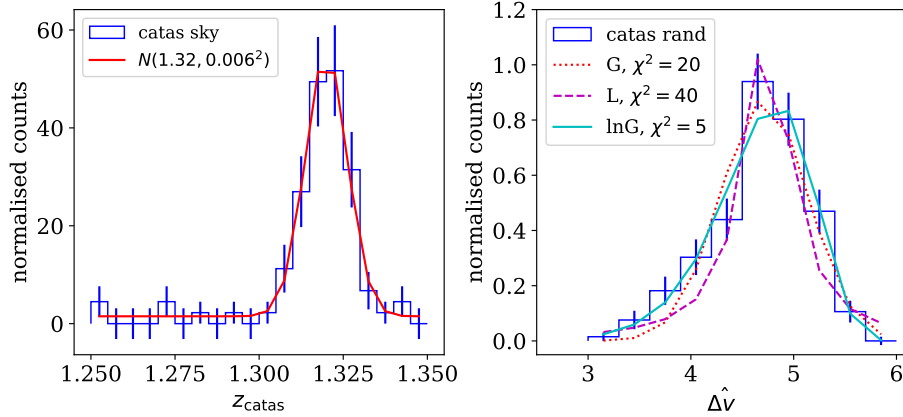


Figure 8. *Left:* The zoom-in histogram of z_{catas} of the sky confusion samples at $1.25 < z < 1.35$ (empty histogram). The solid line is the best-fitting Gaussian function $\mathcal{N}(1.32, 0.006^2)$ with an offset of 0.61. They compose of 24.9% of catastrophics. *Right:* The histogram of $\hat{\Delta v}$ of the random catastrophics (empty histogram with binomial errors). It is fitted by a Gaussian profile (‘G’, the dotted line), a Lorentzian profile (‘L’, the dashed line), and a log-normal profile (‘lnG’, the solid line). The χ^2 improvement brought by the extra 1 parameter of the log-normal distribution is significant. Therefore, $\mathcal{LN}(0.64, 0.25^2, 6.62)$ is the best description of the random catastrophics $\hat{\Delta v}$.

5.2 Modelling the Catastrophics

The z_{true} of sky confusion and random catastrophics both follow the $n(z)$ of the ELG targets (full catalogue) as illustrated in Figure 7. Therefore, we randomly take 0.26% galaxies from the ABACUS-SUMMIT mocks and implement the following pattern to reproduce the realistic catastrophics

$$z_{\text{catas}} = \begin{cases} z_{\text{true}} + \Delta v_{\text{ran}}, & \text{random catastrophics, 76\%;} \\ \mathcal{N}(1.32, 0.006^2), & \text{extra sky confusion, 24\%,} \end{cases} \quad (5.2)$$

where z_{true} is the redshift of ABACUSSUMMIT galaxy mocks. Half of Δv_{ran} is positive and the other half is negative, and $|\Delta v_{\text{ran}}|$ follows $\mathcal{LN}(0.64, 0.25^2, 6.62)$. We also realise a 1% random catastrophics on ABACUSSUMMIT mocks for demonstration purposes. 1% is an upper limit of the ELG catastrophics rate in eBOSS and DESI [17, 75]. In addition, we remove ABACUSSUMMIT ELGs at $1.31 < z < 1.33$, which is the easiest implementation on data if we want to avoid the impact on the sky confusion at $z \approx 1.32$. Given a similar $n_{\text{local}}(z)$ after implementing the catastrophics, the w_{FKP} of samples with z_{catas} is obtained with the $n_{\text{local}}(z_{\text{catas}})$. All the patterns are implemented on 25 realizations of ABACUSSUMMIT galaxy mocks.

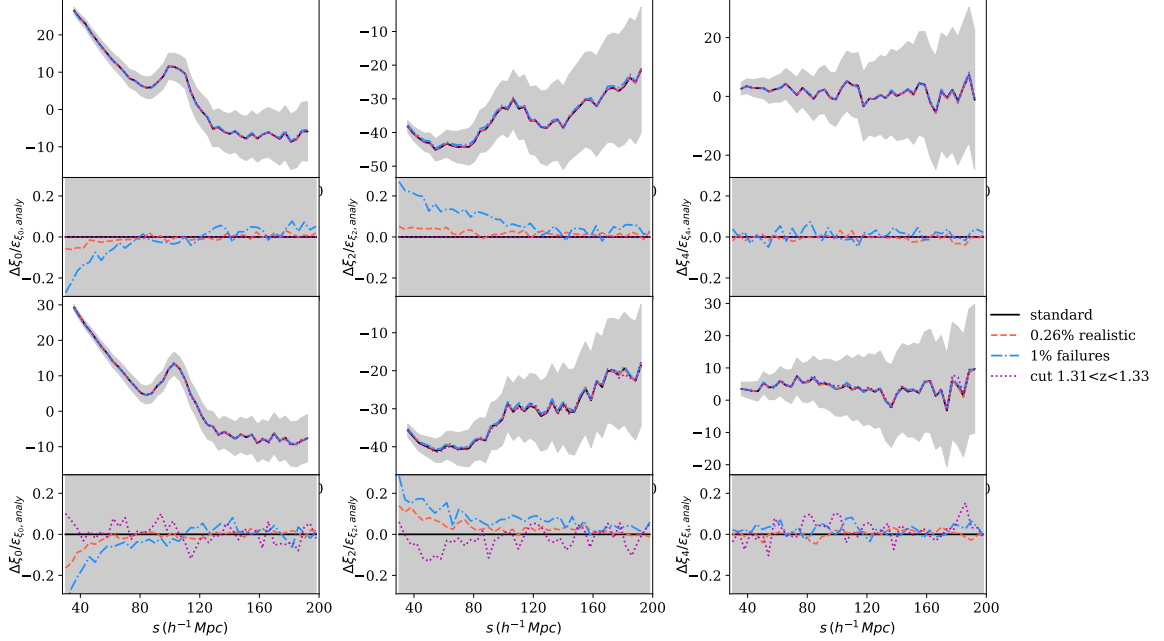


Figure 9. The 2PCF monopole (first column), quadrupole (second column) and hexadecapole (third column) of model galaxies from the standard ABACUSSUMMIT mocks (solid lines), ABACUSSUMMIT mocks with 0.26% realistic catastrophics (dashed lines), ABACUSSUMMIT mocks with hypothetical 1% random catastrophics (dash-dotted lines) and ABACUSSUMMIT mocks without $1.31 < z < 1.33$ (dotted lines). The grey areas are the $1-\varepsilon_\xi$ errors of clustering obtained via analytical covariances (Section 2.2). The first and the second rows are the 2PCF multipoles and the differences between the standard ABACUSSUMMIT mocks and catastrophics/cuts rescaled by the errors provided by the analytical covariance matrices at $0.8 < z < 1.1$. The third and fourth rows are similar but model galaxies at $1.1 < z < 1.6$. Catastrophics lead to negligible clustering effects at $0.8 < z < 1.1$ except for the hypothetical 1% case. For galaxies at $1.1 < z < 1.6$, the realistic 0.26% catastrophics shift the monopole and quadrupole by $> 0.1\varepsilon_\xi$ at $s < 60 h^{-1} \text{Mpc}$, similar to the effects of the hypothetical catastrophics. Hexadecapoles are robust to the catastrophics effect.

5.3 Impact of Catastrophics

We present in Figure 9 and Figure 10 the impact of realistic 0.26% catastrophics, hypothetical 1% random catastrophics and removing ELGs at $1.31 < z < 1.33$ (the sky-confusion-contaminated range) on multipoles of the 2PCF ξ_ℓ and power spectra P_ℓ . Removing ELGs at $1.31 < z < 1.33$ is a possible solution to avoid the impact of the hidden sky confusion at $z \approx 1.32$, corresponding to $f_{\text{catas}} = 2.54\%$.

Their influences are mainly embodied in galaxies at higher redshift $1.1 < z < 1.6$. Realistic and 1% random catastrophics result in up to $0.2\varepsilon_\xi$ impact on ξ_0 and ξ_2 on $s < 60 h^{-1} \text{Mpc}$. The

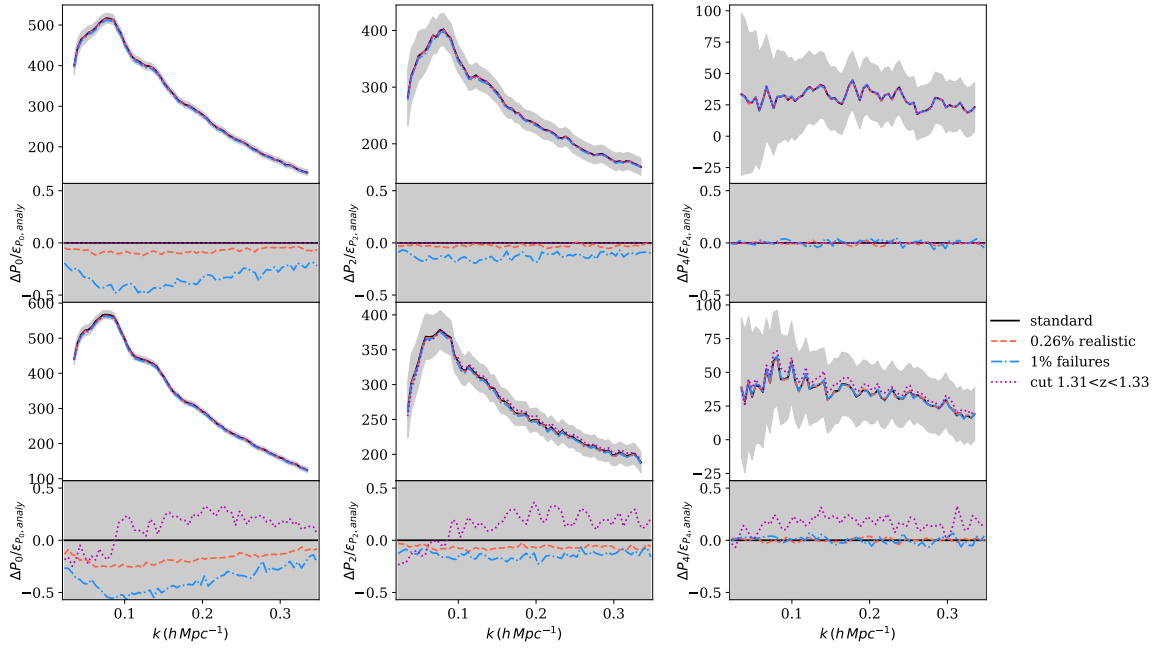


Figure 10. Similar to Figure 9 but for power spectra $P_\ell(k)$ $\ell = 0, 2, 4$.

catastrophics can also suppress the power spectra monopole by up to $0.5\varepsilon_P$. Removing model ELGs at $1.31 < z < 1.33$ slightly perturbs the 2PCF as data and randoms both implemented the truncation. So there is no bias in its 2PCF and the difference from the standard clustering is due to the reduction of galaxies. Removing ELGs boosts the amplitude of ELG P_ℓ at $1.1 < z < 1.6$ by up to $0.3\varepsilon_P$ while the other catastrophics suppress the clustering.

At $0.8 < z < 1.1$, only 1% random catastrophics lead to up to $0.2\varepsilon_\xi$ and $0.5\varepsilon_P$ influence in the configuration space and Fourier space, respectively. This is because the number of galaxies that the realistic catastrophics interferes at $0.8 < z < 1.1$ is too small, and removing galaxies at $1.31 < z < 1.33$ does not affect the LSS at lower redshifts. Hexadecapoles are robust to all three implementations.

Their χ^2_{sys} are presented in Table 2. The DESI BAO analysis focusing on the configuration space will not [28] be influenced by any of the listed catastrophics. This is because the catastrophics do not move the position of the BAO peak. Their maximum χ^2_{sys} (the left column of each χ^2_{sys}) is as small as 0.32. Both lead to negligible changes in the BAO cosmological parameters. However, their impacts become larger in Fourier space at $1.1 < z < 1.6$ due to the systematical shift they cause in the monopole and quadrupole. This could interfere with the RSD measurements. We should remind our reader that all catastrophics and redshift-removal implemented to ABACUSSUMMIT ELG mocks result in the change of window function. The difference in P_ℓ and χ^2_{sys} values is not equivalent to their influence on cosmological measurements. Therefore, we perform cosmological fitting with their corresponding window function to determine how they will interfere with the parameters.

The differences in the best-fitting values of cosmological parameters between the catastrophics clustering and the standard clustering in Fourier space are shown in Table 3 and Table 4. The maximum-likelihood values χ^2/dof (Eq. (3.10)) of all these samples are all smaller than $3.2/59$ as the clustering is calculated from mocks based on accurate N -body simulations and thus is fitted well by theories. Despite the large χ^2_{sys} , the cosmological impacts of all types of systematics are no larger

Space	redshift	$\chi_{\text{sys, realistic}}^2$	$\chi_{\text{sys, random}}^2$	$\chi_{\text{sys, cut}}^2$
Config.	$0.8 < z < 1.1$	0.05	0.33	/
	$1.1 < z < 1.6$	0.1	0.38	0.42
Fourier	$0.8 < z < 1.1$	0.25	4.39	/
	$1.1 < z < 1.6$	1.46	6.66	4.21

Table 2. Similar to Table 1 but for catastrophics models: 0.26% realistic failures, 1% random catastrophics, removing ELGs at $1.31 < z < 1.33$ compared to the ABACUSUMMIT standard clustering. The catastrophics all present larger impacts for ELGs at $1.1 < z < 1.6$. In configuration space, their influence is minor. However, in Fourier space, the catastrophics might bias the cosmological measurement.

than 0.2σ . That is because the nuisance parameters and window functions absorb most of the effects. The nuisance parameters adjust the shape and amplitude of the theoretical curves directly, while the window function influences $P(k)$ through geometric effects. As shown in Figure 11, the clustering difference between the 1% failures and the standard case remains largely unchanged with or without the window function. This suggests that the catastrophics parameters absorb the nuisance effects rather than the window function for the catastrophics-contaminated mocks. In contrast, the clustering difference between the truncated and standard samples varies when the geometric effects (window function) are ignored. This indicates that the clustering changes caused by truncating a slice of the redshift result from changes in geometry. To conclude, the influence of catastrophics effects on DESI ELG in DR1 is not a concern.

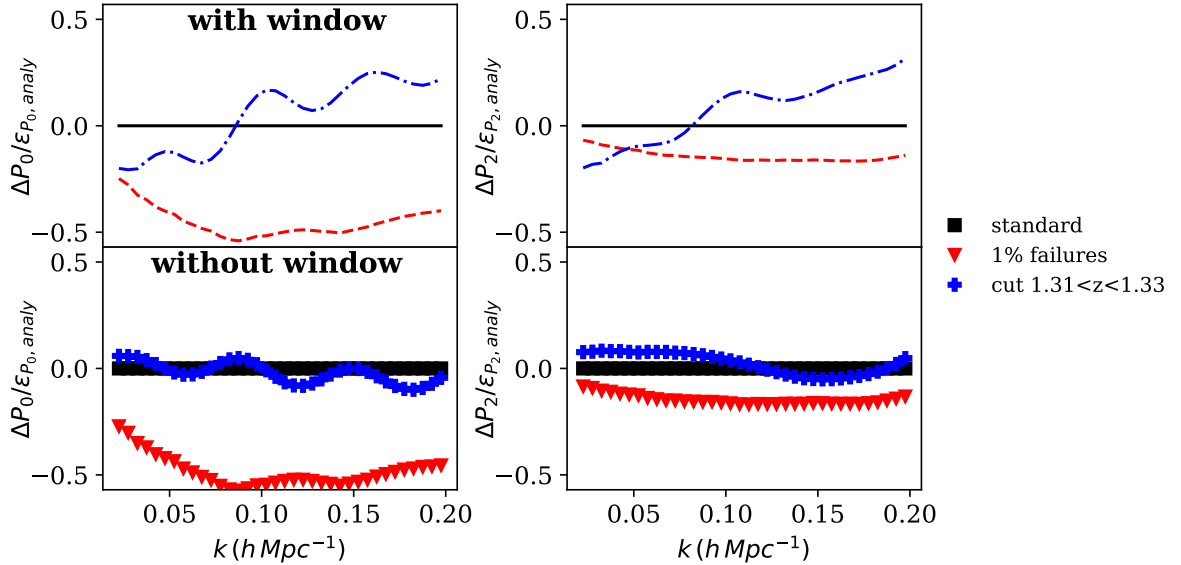


Figure 11. The best-fit theoretical $P(k)$ at $1.1 < z < 1.6$ for the standard clustering (solid lines or squares), the clustering with hypothetical 1% failures (dashed lines or flipped triangles) and the clustering with truncation at $1.31 < z < 1.33$ (dash-dotted lines or plus signs). The first column is the $P(k)$ monopole, and the second is the quadrupole. The upper panel shows the best-fit theoretical curves with window functions applied (i.e., agree with mock $P(k)$), while the lower panel shows the same curves without window functions. The $P(k)$ differences for 1% failures did not shift much without the window function, while that of the cut $1.31 < z < 1.33$ changed its values. This implies that the nuisance parameters absorb the clustering effect of the 1% failures, whereas the truncation effect is primarily accounted for by its window function.

Type	redshift	σ_h	$\sigma_{\omega_{\text{cdm}}}$	σ_{ω_b}	$\sigma_{\log(10^{10}A_s)}$
Realistic	$0.8 < z < 1.1$	0	0	0	0
	$1.1 < z < 1.6$	0.04	0.01	0	0
Random	$0.8 < z < 1.1$	0	0	0	0.06
	$1.1 < z < 1.6$	0.04	0.01	0	0.08
Cut	$0.8 < z < 1.1$	/	/	/	/
	$1.1 < z < 1.6$	0.12	0.05	0	0.17

Table 3. The cosmological impact of catastrophics in full modelling measurements: 0.26% realistic failures, 1% random catastrophics, removing ELGs at $1.31 < z < 1.33$ compared to the ABACUSUMMIT standard clustering. σ represent the 68% confidence level of DESI DR1 cosmological constraints. All influences are smaller than 0.2σ .

Type	redshift	$\sigma_{\alpha_{\text{iso}}}$	$\sigma_{\alpha_{\text{AP}}}$	σ_{df}	σ_{dm}
Realistic	$0.8 < z < 1.1$	0.04	0.03	0.01	0.01
	$1.1 < z < 1.6$	0	0.02	0	0.03
Random	$0.8 < z < 1.1$	0.04	0	0.01	0.1
	$1.1 < z < 1.6$	0.06	0.02	0	0.07
Cut	$0.8 < z < 1.1$	/	/	/	/
	$1.1 < z < 1.6$	0.06	0.04	0.04	0.14

Table 4. Similar to Table 3 but for ShapeFit results. The cosmological impacts are all smaller than 0.2σ .

5.4 Redshift Uncertainty

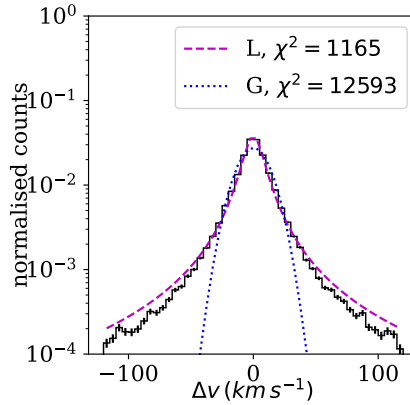


Figure 12. The distribution of DR1 ELG redshift difference Δv (histogram with binomial error bars) that are smaller than 1000 km s^{-1} . There are the best-fit Gaussian profile $\mathcal{N}(0.06, 12.7^2)$ ('G', the dotted line) and Lorentzian profile $\mathcal{L}(0.03, 8.5)$ ('L', the dashed line). The Lorentzian profile is a better description of the ELG redshift uncertainty than a Gaussian profile.

Repeated observations at $0.8 < z < 1.6$ with $|\Delta v| < 1000 \text{ km s}^{-1}$ are used to measure the redshift uncertainty of ELGs as shown in Figure 12. Compared to a Gaussian profile, a Lorentzian

profile described as follows is a better model of DR1 ELG Δv distribution

$$\mathcal{L}(p, w_{\Delta v}) = \frac{A}{1 + ((x - p)/w_{\Delta v})^2}. \quad (5.3)$$

where $A = 0.04$, $p = 0.03$ and $w_{\Delta v} = 8.5 \text{ km s}^{-1}$. This $w_{\Delta v}$ is similar to the values of the visual inspection and survey validation programs for DESI ELGs [17, 52] that are at the level of $\sim 10 \text{ km s}^{-1}$, thus its impact on the DR1 ELG clustering is negligible on $s > 5 h^{-1} \text{ Mpc}$ [53]. Its percentile velocities at 50, 95, and 99.5 % are 8.2, 53.5 and 139.0 km s^{-1} , respectively. They are less than half of the values from eBOSS ELGs, which are 20, 100, and 300 km s^{-1} [5] thanks to the improvement of spectrographs and redshift pipeline [11, 36, 37].

6 Conclusion

In this paper, we investigate the spectroscopic systematics of ELGs in DESI DR1 and their clustering impact on 2PCF $\xi(s)$ and the power spectrum $P(k)$. Spectroscopic systematics arise from the failed redshift measurements and cause non-cosmological variations in the galaxy distribution. One of the aspects is the redshift success rate f_{goodz} dependences on the observing conditions. The other ones are collective effects introduced by the catastrophics and the redshift uncertainty in the redshift measurement.

The actual f_{goodz} depends on the squared signal-to-noise for ELG spectra TSNR2_ELG ($S_{\text{spec,obs}}$) and redshift z , leading to larger f_{goodz} for ELGs with larger $S_{\text{spec,obs}}$ at different redshift bins. This is equivalent to unfairly up-weighting ELGs with high $S_{\text{spec,obs}}$. We develop the redshift failure weight w_{zfail} as the inverse of a linear function of $S_{\text{spec,obs}}$ as a function of $(S_{\text{spec,obs}}, z)$. With w_{zfail} , we successfully recover a close-to-unity $f_{\text{goodz}}-S_{\text{spec,obs}}$ relation for ELGs at fine redshift bins with $dz = 0.1$. However, this weight is imperfect since there is no information for f_{goodz} variations on the focal plane. Therefore, the f_{goodz} dependencies on the distance from the focal centre, and the fibre aperture loss at G, R, and Z bands, do not show improvement after applying w_{zfail} . We thus create fibre-based corrections η_{zfail} on the w_{zfail} . η_{zfail} is the inverse of the w_{zfail} -weighted f_{goodz} for each fibre. Implementing η_{zfail} leads to a more uniform $f_{\text{goodz}}-S_{\text{spec,obs}}$ relation and a unity relation between f_{goodz} , the distance to the focal plane, and all the throughput in different bands. Due to the small f_{goodz} difference before any corrections, w_{zfail} and $w_{\text{zfail}}\eta_{\text{zfail}}$ result in smaller than $0.05\epsilon_\xi$ in the monopole, quadrupole, and hexadecapole of ξ and $P(k)$, corresponding to less than $\chi_{\text{sys}}^2 = 0.25$ differences. It means that their cosmological influences are negligible.

Catastrophics and redshift uncertainty are systematics that are difficult to subtract from individual targets. They can be explored through repeated observations with the redshift difference Δv , and their clustering impact can be modelled in cosmological theories. The catastrophics rate of DESI DR1 ELGs is 0.26%, similar to that of ELGs from DESI survey validation and eBOSS. There are five types of failure patterns: sky confusions that result in $z_{\text{catas}} \approx 1.32$ (26.7%), other misidentification between sky-emission residuals and [O II] doublets (27.6%), double objects (22%), double failures (12.1%), and other failures (11.6%).

Despite the variety of the patterns, we can model their $z_{\text{catas}}-z_{\text{true}}$ relation in the ABACUSSUMMIT galaxy mocks with 75.1% of random catastrophics and 24.9% of the excess sky confusions besides the random catastrophics (realistic catastrophics). We also generate catastrophics-contaminated galaxy mocks with a hypothetical with 1% random catastrophics and mocks without the sky-confusion-contaminated redshift range $1.31 < z < 1.33$. Their impacts on the 2PCF are as small as $0.3\epsilon_\xi$ for all multipoles at $0.8 < z < 1.6$, corresponding to $\chi_{\text{sys}}^2 < 1$. Therefore, we do not expect catastrophics to affect the BAO and RSD measurement in the configuration space. However, realistic failures and

1% random catastrophics systematically suppress the power spectra by up to $0.5\epsilon_P$ at both redshift bins. Removing the contaminated shell of $1.31 < z < 1.33$ from the data is a simple solution to avoid bias in cosmological measurements based on the configuration space. In the Fourier space, removing a small shell of the observed 3D map boosts the monopole by $0.3\epsilon_P$ at $1.1 < z < 1.6$. All these lead to χ_{sys}^2 values larger than 1 in Fourier space. We calculate the new window function of all three mocks and do RSD fitting with full-modelling and ShapeFit compression. We find that the cosmological influence of the realistic catastrophics, the hypothetical 1% catastrophics and removing the contaminated $1.31 < z < 1.33$ are smaller than 0.2σ . This means that the deviation from the standard P_ℓ is mainly from the change of geometry and nuisance parameters. This level of systematics is also within the systematics budget of [30].

In conclusion, the spectroscopic systematics of ELGs have a minor impact on DESI cosmological measurements. Nevertheless, any unexpected patterns in this type of systematics are still worth examining. The modelling of f_{goodz} needs to take into account the information on the focal plane as well despite the small variations. The catastrophics, composed of 0.26% of the ELGs, have minor impacts on the cosmological parameters. This is not problematic for the current redshift surveys, but it can be a problem for photometric surveys from space. The redshift uncertainty of ELGs is small thanks to the characteristic [O II] doublet. But that of the Lyman-Alpha Emitters (LAEs), as a type of emission-line galaxies, though, might be more complicated. With more data and improved telescopes, we will be able to resolve all these issues before they become a significant problem.

Data Availability

The data used in this analysis will be made public along the Data Release 1 (details in <https://data.desi.lbl.gov/doc/releases/>). Zenodo includes all data to reproduce the figures in this paper: <https://doi.org/10.5281/zenodo.11302697>.

Acknowledgments

JY, DFS, and JPK acknowledge the support from the SNF 200020_175751 and 200020_207379 ‘‘Cosmology with 3D Maps of the Universe’’ research grant. We would like to thank Anand Raichoor, Allyson Brodzeller, Ruiyang Zhao and Julien Guy for their helpful discussions. We also would like to thank Andrei Variu for his support in visualising DESI spectra.

This material is based upon work supported by the U.S. Department of Energy (DOE), Office of Science, Office of High-Energy Physics, under Contract No. DE-AC02-05CH11231, and by the National Energy Research Scientific Computing Center, a DOE Office of Science User Facility under the same contract. Additional support for DESI was provided by the U.S. National Science Foundation (NSF), Division of Astronomical Sciences under Contract No. AST-0950945 to the NSF’s National Optical-Infrared Astronomy Research Laboratory; the Science and Technology Facilities Council of the United Kingdom; the Gordon and Betty Moore Foundation; the Heising-Simons Foundation; the French Alternative Energies and Atomic Energy Commission (CEA); the National Council of Humanities, Science and Technology of Mexico (CONAHCYT); the Ministry of Science and Innovation of Spain (MICINN), and by the DESI Member Institutions: <https://www.desi.lbl.gov/collaborating-institutions>. Any opinions, findings, and conclusions or recommendations expressed in this material are those of the author(s) and do not necessarily reflect the views of the U. S. National Science Foundation, the U. S. Department of Energy, or any of the listed funding agencies.

The authors are honored to be permitted to conduct scientific research on Iolkam Du’ag (Kitt Peak), a mountain with particular significance to the Tohono O’odham Nation.

A Visualise Spectra of ELG Catastrophics

We present the ELG spectra of sky confusion at $z_{\text{catas}} \approx 1.32$, sky confusion at other redshifts, double objects in the spectra, totally failed redshift measurements, and the misidentification of $H\alpha$ to be an $[\text{O II}]$ doublet in Figure 13 as introduced in Section 5.1. The insert subplots in the first, second and fifth spectra are enlarged spectral lines. The subplot on the left shows the spectra around the true $[\text{O II}]$ doublet (black solid lines with blue dashed vertical lines for $[\text{O II}]$) and the one on the right is the false $[\text{O II}]$ line that results in catastrophics. The physical $[\text{O II}]$ emission lines for the left subplot in the first and the second spectra differ from the sky residuals in the right subplot. The $H\alpha$ emission in the right subplot of the fifth spectra was also different from the $[\text{O II}]$ doublet. However, REDROCK was unable to distinguish them for some reason. Both redshift measurements are true in the third spectrum: one is determined by multiple emission lines from the $z_0 = 0$ object, and the other is from $[\text{O II}]$ emission. In the fourth spectra, both redshift measurements are wrong as they regard sky residuals at different redshifts as $[\text{O II}]$ doublets. All of them pass the good-redshift selection and most of them are within $0.8 < z < 1.6$ redshift range. This indicates that the 0.26% is probably a lower limit of the catastrophics rate because there can be consistently wrong redshift measurements that pass the good-redshift criteria hidden in the current catalogue.

B Catastrophics Impacts on Small-Scale 2PCF

In Section 5, we demonstrate that the impact of catastrophics on cosmological scales in the configuration space is negligible. In this section, we discuss the influence of catastrophics on small scales as it has not been corrected in the current clustering. As the analytical covariance is no longer applicable at $s < 20 h^{-1}$ Mpc, we used the jackknife error from the EDR ELG samples calculated with 128 subsamples using PYCORR in our discussion. At $1.1 < z < 1.6$, the catastrophics can suppress the monopole by up to $\sim 0.5\epsilon_{\mathcal{E}}$ and change quadrupole systematically as shown in Figure 14. This indicates that the galaxy-halo connection studies of ELGs in galaxy surveys, with HOD or SubHalo Abundance Matching (SHAM), may need to consider this effect when they fit the observed ELG clustering at small scales.

C Author Affiliations

¹Institute of Physics, Laboratory of Astrophysics, École Polytechnique Fédérale de Lausanne (EPFL), Observatoire de Sauverny, CH-1290 Versoix, Switzerland

²Center for Cosmology and AstroParticle Physics, The Ohio State University, 191 West Woodruff Avenue, Columbus, OH 43210, USA

³Department of Astronomy, The Ohio State University, 4055 McPherson Laboratory, 140 W 18th Avenue, Columbus, OH 43210, USA

⁴The Ohio State University, Columbus, 43210 OH, USA

⁵Université Paris-Saclay, CEA, IRFU, F-91191 Gif-sur-Yvette, France

⁶University of Michigan, Ann Arbor, MI 48109, USA

⁷Aix Marseille Université, CNRS, LAM (Laboratoire d’Astrophysique de Marseille) UMR 7326, F13388, Marseille, France

- ⁸Department of Physics and Astronomy, University of Waterloo, 200 University Ave W, Waterloo, ON N2L 3G1, Canada
- ⁹Perimeter Institute for Theoretical Physics, 31 Caroline St. North, Waterloo, ON N2L 2Y5, Canada
- ¹⁰Waterloo Centre for Astrophysics, University of Waterloo, 200 University Ave W, Waterloo, ON N2L 3G1, Canada
- ¹¹Graduate Institute of Astrophysics and Department of Physics, National Taiwan University, No. 1, Sec. 4, Roosevelt Rd., Taipei 10617, Taiwan
- ¹²Center for Astrophysics | Harvard & Smithsonian, 60 Garden Street, Cambridge, MA 02138, USA
- ¹³Lawrence Berkeley National Laboratory, 1 Cyclotron Road, Berkeley, CA 94720, USA
- ¹⁴Physics Dept., Boston University, 590 Commonwealth Avenue, Boston, MA 02215, USA
- ¹⁵Department of Physics & Astronomy, University College London, Gower Street, London, WC1E 6BT, UK
- ¹⁶Instituto de Física, Universidad Nacional Autónoma de México, Cd. de México C.P. 04510, México
- ¹⁷NSF NOIRLab, 950 N. Cherry Ave., Tucson, AZ 85719, USA
- ¹⁸Department of Physics & Astronomy and Pittsburgh Particle Physics, Astrophysics, and Cosmology Center (PITT PACC), University of Pittsburgh, 3941 O'Hara Street, Pittsburgh, PA 15260, USA
- ¹⁹Kavli Institute for Particle Astrophysics and Cosmology, Stanford University, Menlo Park, CA 94305, USA
- ²⁰SLAC National Accelerator Laboratory, Menlo Park, CA 94305, USA
- ²¹Departamento de Física, Universidad de los Andes, Cra. 1 No. 18A-10, Edificio Ip, CP 111711, Bogotá, Colombia
- ²²Observatorio Astronómico, Universidad de los Andes, Cra. 1 No. 18A-10, Edificio H, CP 111711 Bogotá, Colombia
- ²³Institut d'Estudis Espacials de Catalunya (IEEC), 08034 Barcelona, Spain
- ²⁴Institute of Cosmology and Gravitation, University of Portsmouth, Dennis Sciama Building, Portsmouth, PO1 3FX, UK
- ²⁵Institute of Space Sciences, ICE-CSIC, Campus UAB, Carrer de Can Magrans s/n, 08913 Bellaterra, Barcelona, Spain
- ²⁶Department of Physics, The Ohio State University, 191 West Woodruff Avenue, Columbus, OH 43210, USA
- ²⁷School of Mathematics and Physics, University of Queensland, 4072, Australia
- ²⁸Sorbonne Université, CNRS/IN2P3, Laboratoire de Physique Nucléaire et de Hautes Energies (LPNHE), FR-75005 Paris, France
- ²⁹Departament de Física, Serra Hünter, Universitat Autònoma de Barcelona, 08193 Bellaterra (Barcelona), Spain
- ³⁰Institut de Física d'Altes Energies (IFAE), The Barcelona Institute of Science and Technology, Campus UAB, 08193 Bellaterra Barcelona, Spain
- ³¹Institució Catalana de Recerca i Estudis Avançats, Passeig de Lluís Companys, 23, 08010 Barcelona, Spain
- ³²Department of Physics and Astronomy, Siena College, 515 Loudon Road, Loudonville, NY 12211, USA
- ³³Department of Physics and Astronomy, University of Sussex, Brighton BN1 9QH, U.K
- ³⁴Department of Physics & Astronomy, University of Wyoming, 1000 E. University, Dept. 3905, Laramie, WY 82071, USA
- ³⁵National Astronomical Observatories, Chinese Academy of Sciences, A20 Datun Rd., Chaoyang District, Beijing, 100012, P.R. China
- ³⁶Departamento de Física, Universidad de Guanajuato - DCI, C.P. 37150, Leon, Guanajuato, México

- ³⁷Instituto Avanzado de Cosmología A. C., San Marcos 11 - Atenas 202. Magdalena Contreras, 10720. Ciudad de México, México
- ³⁸Space Sciences Laboratory, University of California, Berkeley, 7 Gauss Way, Berkeley, CA 94720, USA
- ³⁹University of California, Berkeley, 110 Sproul Hall #5800 Berkeley, CA 94720, USA
- ⁴⁰Instituto de Astrofísica de Andalucía (CSIC), Glorieta de la Astronomía, s/n, E-18008 Granada, Spain
- ⁴¹Department of Physics, Kansas State University, 116 Cardwell Hall, Manhattan, KS 66506, USA
- ⁴²Department of Physics and Astronomy, Sejong University, Seoul, 143-747, Korea
- ⁴³CIEMAT, Avenida Complutense 40, E-28040 Madrid, Spain
- ⁴⁴Space Telescope Science Institute, 3700 San Martin Drive, Baltimore, MD 21218, USA
- ⁴⁵Department of Physics, University of Michigan, Ann Arbor, MI 48109, USA
- ⁴⁶Department of Physics & Astronomy, Ohio University, Athens, OH 45701, USA
- ⁴⁷Department of Astronomy, Tsinghua University, 30 Shuangqing Road, Haidian District, Beijing, China, 100190

References

- [1] D.J. Eisenstein and W. Hu, *Baryonic Features in the Matter Transfer Function*, *Astrophys. J.* **496** (1998) 605 [[astro-ph/9709112](#)].
- [2] N. Kaiser, *Clustering in real space and in redshift space*, *Mon. Nat. Roy. Astron. Soc.* **227** (1987) 1.
- [3] C. Blake, S. Brough, M. Colless, W. Couch, S. Croom, T. Davis et al., *The WiggleZ Dark Energy Survey: the selection function and $z = 0.6$ galaxy power spectrum*, *Mon. Nat. Roy. Astron. Soc.* **406** (2010) 803 [[1003.5721](#)].
- [4] A.J. Ross, F. Beutler, C.-H. Chuang, M. Pellejero-Ibanez, H.-J. Seo, M. Vargas-Magaña et al., *The clustering of galaxies in the completed SDSS-III Baryon Oscillation Spectroscopic Survey: observational systematics and baryon acoustic oscillations in the correlation function*, *Mon. Nat. Roy. Astron. Soc.* **464** (2017) 1168 [[1607.03145](#)].
- [5] A. Raichoor, A. de Mattia, A.J. Ross, C. Zhao, S. Alam, S. Avila et al., *The completed SDSS-IV extended Baryon Oscillation Spectroscopic Survey: large-scale structure catalogues and measurement of the isotropic BAO between redshift 0.6 and 1.1 for the Emission Line Galaxy Sample*, *Mon. Nat. Roy. Astron. Soc.* **500** (2021) 3254 [[2007.09007](#)].
- [6] A. Tamone, A. Raichoor, C. Zhao, A. de Mattia, C. Gorgoni, E. Burtin et al., *The completed SDSS-IV extended baryon oscillation spectroscopic survey: growth rate of structure measurement from anisotropic clustering analysis in configuration space between redshift 0.6 and 1.1 for the emission-line galaxy sample*, *Mon. Nat. Roy. Astron. Soc.* **499** (2020) 5527 [[2007.09009](#)].
- [7] A. de Mattia, V. Ruhlmann-Kleider, A. Raichoor, A.J. Ross, A. Tamone, C. Zhao et al., *The completed SDSS-IV extended Baryon Oscillation Spectroscopic Survey: measurement of the BAO and growth rate of structure of the emission line galaxy sample from the anisotropic power spectrum between redshift 0.6 and 1.1*, *Mon. Nat. Roy. Astron. Soc.* **501** (2021) 5616 [[2007.09008](#)].
- [8] M. Levi, C. Bebek, T. Beers, R. Blum, R. Cahn, D. Eisenstein et al., *The DESI Experiment, a whitepaper for Snowmass 2013*, *arXiv e-prints* (2013) [arXiv:1308.0847](#) [[1308.0847](#)].
- [9] DESI Collaboration, A. Amir, J. Aguilar, S. Ahlen, S. Alam, L.E. Allen et al., *The desi experiment part i: Science, targeting, and survey design*, 2016.
- [10] DESI Collaboration, A. Aghamousa, J. Aguilar, S. Ahlen, S. Alam, L.E. Allen et al., *The DESI Experiment Part II: Instrument Design*, Oct., 2016.

- [11] DESI Collaboration, B. Abareshi, J. Aguilar, S. Ahlen, S. Alam, D.M. Alexander et al., *Overview of the Instrumentation for the Dark Energy Spectroscopic Instrument*, *Astron. J.* **164** (2022) 207 [2205.10939].
- [12] DESI Collaboration, A.G. Adame, J. Aguilar, S. Ahlen, S. Alam, G. Aldering et al., *The Early Data Release of the Dark Energy Spectroscopic Instrument*, *Astron. J.* **168** (2024) 58 [2306.06308].
- [13] DESI Collaboration, A.G. Adame, J. Aguilar, S. Ahlen, S. Alam, G. Aldering et al., *Validation of the Scientific Program for the Dark Energy Spectroscopic Instrument*, *Astron. J.* **167** (2024) 62 [2306.06307].
- [14] DESI Collaboration, *DESI 2024 I: Data Release 1 of the Dark Energy Spectroscopic Instrument*, in preparation (2025) .
- [15] C. Hahn, M.J. Wilson, O. Ruiz-Macias, S. Cole, D.H. Weinberg, J. Moustakas et al., *The DESI Bright Galaxy Survey: Final Target Selection, Design, and Validation*, *Astron. J.* **165** (2023) 253 [2208.08512].
- [16] R. Zhou, B. Dey, J.A. Newman, D.J. Eisenstein, K. Dawson, S. Bailey et al., *Target Selection and Validation of DESI Luminous Red Galaxies*, *Astron. J.* **165** (2023) 58 [2208.08515].
- [17] A. Raichoor, J. Moustakas, J.A. Newman, T. Karim, S. Ahlen, S. Alam et al., *Target Selection and Validation of DESI Emission Line Galaxies*, *Astron. J.* **165** (2023) 126 [2208.08513].
- [18] E. Chaussidon, C. Yèche, N. Palanque-Delabrouille, D.M. Alexander, J. Yang, S. Ahlen et al., *Target Selection and Validation of DESI Quasars*, *Astrophys. J.* **944** (2023) 107 [2208.08511].
- [19] DESI Collaboration, *DESI 2024 II: Sample definitions, characteristics and two-point clustering statistics*, in preparation (2024) .
- [20] A.J. Ross, J. Aguilar, S. Ahlen, S. Alam, A. Anand, S. Bailey et al., *The Construction of Large-scale Structure Catalogs for the Dark Energy Spectroscopic Instrument*, *arXiv e-prints* (2024) arXiv:2405.16593 [2405.16593].
- [21] DESI Collaboration, A.G. Adame, J. Aguilar, S. Ahlen, S. Alam, D.M. Alexander et al., *DESI 2024 IV: Baryon Acoustic Oscillations from the Lyman Alpha Forest*, *arXiv e-prints* (2024) arXiv:2404.03001 [2404.03001].
- [22] C. Zhao et al., *Mock catalogues with survey realism for the DESI DR1*, in preparation (2024) .
- [23] F. Prada et al., *Covariance errors from GLAM N-body simulations for DESI 2024*, in preparation (2024) .
- [24] O. Alves et al., *Analytical covariance matrices of DESI galaxy power spectra*, in preparation (2024) .
- [25] M. Rashkovetskiy, D. Forero-Sánchez, A. de Mattia, D.J. Eisenstein, N. Padmanabhan, H. Seo et al., *Semi-analytical covariance matrices for two-point correlation function for DESI 2024 data*, *arXiv e-prints* (2024) arXiv:2404.03007 [2404.03007].
- [26] D. Forero-Sanchez et al., *Analytical and EZmock covariance validation for the DESI 2024 results*, in preparation (2024) .
- [27] U. Andrade, J. Mena-Fernández, H. Awan, A.J. Ross, S. Brieden, J. Pan et al., *Validating the Galaxy and Quasar Catalog-Level Blinding Scheme for the DESI 2024 analysis*, *arXiv e-prints* (2024) arXiv:2404.07282 [2404.07282].
- [28] DESI Collaboration, A.G. Adame, J. Aguilar, S. Ahlen, S. Alam, D.M. Alexander et al., *DESI 2024 III: Baryon Acoustic Oscillations from Galaxies and Quasars*, *arXiv e-prints* (2024) arXiv:2404.03000 [2404.03000].
- [29] S. Alam, M. Aubert, S. Avila, C. Balland, J.E. Bautista, M.A. Bershadsky et al., *Completed SDSS-IV extended Baryon Oscillation Spectroscopic Survey: Cosmological implications from two decades of spectroscopic surveys at the Apache Point Observatory*, *Phys. Rev. D* **103** (2021) 083533 [2007.08991].

- [30] DESI Collaboration, *DESI 2024 V: Analysis of the full shape of two-point clustering statistics from galaxies and quasars*, in preparation (2024) .
- [31] DESI Collaboration, A.G. Adame, J. Aguilar, S. Ahlen, S. Alam, D.M. Alexander et al., *DESI 2024 VI: Cosmological Constraints from the Measurements of Baryon Acoustic Oscillations*, [arXiv e-prints \(2024\) arXiv:2404.03002 \[2404.03002\]](#).
- [32] DESI Collaboration, *DESI 2024 VII: Cosmological constraints from full-shape analyses of the two-point clustering statistics measurements*, in preparation (2024) .
- [33] DESI Collaboration, *Constraints on Primordial Non-Gaussianities for DESI 2024*, in preparation (2024) .
- [34] A.D. Myers, J. Moustakas, S. Bailey, B.A. Weaver, A.P. Cooper, J.E. Forero-Romero et al., *The Target-selection Pipeline for the Dark Energy Spectroscopic Instrument*, *Astron. J.* **165** (2023) 50 [2208.08518].
- [35] Raichoor et al., in preparation (2024) .
- [36] J. Guy, S. Bailey, A. Kremin, S. Alam, D.M. Alexander, C. Allende Prieto et al., *The Spectroscopic Data Processing Pipeline for the Dark Energy Spectroscopic Instrument*, *Astron. J.* **165** (2023) 144 [2209.14482].
- [37] Bailey et al., in preparation (2024) .
- [38] Schlegel et al., in preparation (2024) .
- [39] H. Zou, X. Zhou, X. Fan, T. Zhang, Z. Zhou, J. Nie et al., *Project Overview of the Beijing-Arizona Sky Survey*, *Publ. Astron. Soc. Pac* **129** (2017) 064101 [1702.03653].
- [40] A. Dey, D.J. Schlegel, D. Lang, R. Blum, K. Burleigh, X. Fan et al., *Overview of the DESI Legacy Imaging Surveys*, *Astron. J.* **157** (2019) 168 [1804.08657].
- [41] The Dark Energy Survey Collaboration, *The Dark Energy Survey*, [arXiv e-prints \(2005\) astro/astro-ph/0510346](#).
- [42] B. Flaugher, H.T. Diehl, K. Honscheid, T.M.C. Abbott, O. Alvarez, R. Angstadt et al., *The Dark Energy Camera*, *Astron. J.* **150** (2015) 150 [1504.02900].
- [43] A. Rosado-Marin et al., *Mitigating Imaging Systematics for DESI DR1 Emission Line Galaxies and Beyond*, in preparation (2024) .
- [44] H. Kong, A.J. Ross, K. Honscheid, D. Lang, A. Porredon, A. de Mattia et al., *Forward modeling fluctuations in the DESI LRGs target sample using image simulations*, [arXiv e-prints \(2024\) arXiv:2405.16299 \[2405.16299\]](#).
- [45] R. Zhou et al., in preparation (2024) .
- [46] E. Chaussidon, A. de Mattia, C. Yèche, J. Aguilar, S. Ahlen, D. Brooks et al., *Blinding scheme for the scale-dependence bias signature of local primordial non-Gaussianity for DESI 2024*, [arXiv e-prints \(2024\) arXiv:2406.00191 \[2406.00191\]](#).
- [47] D. Bianchi et al., *Characterization of DESI fiber assignment incompleteness effect on 2-point clustering and mitigation methods for 2024 analysis*, in preparation (2024) .
- [48] J. Lasker, A.C. Rosell, A.D. Myers, A.J. Ross, D. Bianchi, M.M.S. Hanif et al., *Production of Alternate Realizations of DESI Fiber Assignment for Unbiased Clustering Measurement in Data and Simulations*, [arXiv e-prints \(2024\) arXiv:2404.03006 \[2404.03006\]](#).
- [49] M. M. S Hanif et al., *Fast Fiber Assign: Emulating fiber assignment effects for realistic DESI catalogs*, in preparation (2024) .
- [50] M. Pinon, A. de Mattia, P. McDonald, E. Burtin, V. Ruhlmann-Kleider, M. White et al., *Mitigation of DESI fiber assignment incompleteness effect on two-point clustering with small angular scale truncated estimators*, [arXiv e-prints \(2024\) arXiv:2406.04804 \[2406.04804\]](#).

- [51] A. Krolewski, J. Yu, A.J. Ross, S. Penmetsa, W.J. Percival, R. Zhou et al., *Impact and mitigation of spectroscopic systematics on DESI DR1 clustering measurements*, *arXiv e-prints* (2024) [arXiv:2405.17208](https://arxiv.org/abs/2405.17208) [2405.17208].
- [52] T.-W. Lan, R. Tojeiro, E. Armengaud, J.X. Prochaska, T.M. Davis, D.M. Alexander et al., *The DESI Survey Validation: Results from Visual Inspection of Bright Galaxies, Luminous Red Galaxies, and Emission-line Galaxies*, *Astrophys. J.* **943** (2023) 68 [2208.08516].
- [53] J. Yu, C. Zhao, V. Gonzalez-Perez, C.-H. Chuang, A. Brodzeller, A. de Mattia et al., *The DESI One-Percent Survey: exploring a generalized SHAM for multiple tracers with the UNIT simulation*, *Mon. Nat. Roy. Astron. Soc.* **527** (2024) 6950 [2306.06313].
- [54] Planck Collaboration, N. Aghanim, Y. Akrami, M. Ashdown, J. Aumont, C. Baccigalupi et al., *Planck 2018 results. VI. Cosmological parameters*, *Astron. Astrophys.* **641** (2020) A6 [1807.06209].
- [55] A. Rocher, V. Ruhlmann-Kleider, E. Burtin, S. Yuan, A. de Mattia, A.J. Ross et al., *The DESI One-Percent survey: exploring the Halo Occupation Distribution of Emission Line Galaxies with ABACUSSUMMIT simulations*, *JCAP* **2023** (2023) 016 [2306.06319].
- [56] N.A. Maksimova, L.H. Garrison, D.J. Eisenstein, B. Hadzhiyska, S. Bose and T.P. Satterthwaite, *ABACUSSUMMIT: a massive set of high-accuracy, high-resolution N-body simulations*, *Mon. Nat. Roy. Astron. Soc.* **508** (2021) 4017 [2110.11398].
- [57] D. Wadekar and R. Scoccimarro, *Galaxy power spectrum multipoles covariance in perturbation theory*, *Phys. Rev. D* **102** (2020) 123517 [1910.02914].
- [58] M. Rashkovetskiy, D.J. Eisenstein, J.N. Aguilar, D. Brooks, T. Claybaugh, S. Cole et al., *Validation of semi-analytical, semi-empirical covariance matrices for two-point correlation function for early DESI data*, *Mon. Nat. Roy. Astron. Soc.* **524** (2023) 3894 [2306.06320].
- [59] H.A. Feldman, N. Kaiser and J.A. Peacock, *Power-Spectrum Analysis of Three-dimensional Redshift Surveys*, *Astrophys. J.* **426** (1994) 23 [astro-ph/9304022].
- [60] S.D. Landy and A.S. Szalay, *Bias and Variance of Angular Correlation Functions*, *Astrophys. J.* **412** (1993) 64.
- [61] M. Sinha and L.H. Garrison, *CORRFUNC - a suite of blazing fast correlation functions on the CPU*, *Mon. Nat. Roy. Astron. Soc.* **491** (2020) 3022.
- [62] M. Sinha and L. Garrison, *Corrfunc: Blazing fast correlation functions with avx512f simd intrinsics*, in *Software Challenges to Exascale Computing*, A. Majumdar and R. Arora, eds., (Singapore), pp. 3–20, Springer Singapore, 2019, https://doi.org/10.1007/978-981-13-7729-7_1.
- [63] K. Yamamoto, M. Nakamichi, A. Kamino, B.A. Bassett and H. Nishioka, *A Measurement of the Quadrupole Power Spectrum in the Clustering of the 2dF QSO Survey*, *Pub. Astron. Soc. Japan* **58** (2006) 93 [astro-ph/0505115].
- [64] N. Hand, Y. Li, Z. Slepian and U. Seljak, *An optimal FFT-based anisotropic power spectrum estimator*, *JCAP* **2017** (2017) 002 [1704.02357].
- [65] M. Maus, S. Chen, M. White, J. Aguilar, S. Ahlen, A. Aviles et al., *An analysis of parameter compression and full-modeling techniques with Velocileptors for DESI 2024 and beyond*, *arXiv e-prints* (2024) [arXiv:2404.07312](https://arxiv.org/abs/2404.07312) [2404.07312].
- [66] H.E. Noriega, A. Aviles, H. Gil-Marín, S. Ramirez-Solano, S. Fromenteau, M. Vargas-Magaña et al., *Comparing Compressed and Full-modeling Analyses with FOLPS: Implications for DESI 2024 and beyond*, *arXiv e-prints* (2024) [arXiv:2404.07269](https://arxiv.org/abs/2404.07269) [2404.07269].
- [67] Y. Lai, C. Howlett, M. Maus, H. Gil-Marín, H.E. Noriega, S. Ramírez-Solano et al., *A comparison between Shapefit compression and Full-Modelling method with PyBird for DESI 2024 and beyond*, *arXiv e-prints* (2024) [arXiv:2404.07283](https://arxiv.org/abs/2404.07283) [2404.07283].

- [68] S. Ramirez-Solano, M. Icaza-Lizaola, H.E. Noriega, M. Vargas-Magaña, S. Fromenteau, A. Aviles et al., *Full Modeling and Parameter Compression Methods in configuration space for DESI 2024 and beyond*, *arXiv e-prints* (2024) arXiv:2404.07268 [2404.07268].
- [69] D. Blas, J. Lesgourgues and T. Tram, *The cosmic linear anisotropy solving system (class). part ii: Approximation schemes*, *Journal of Cosmology and Astroparticle Physics* **2011** (2011) 034.
- [70] A. Lewis, A. Challinor and A. Lasenby, *Efficient computation of cosmic microwave background anisotropies in closed friedmann-robertson-walker models*, *The Astrophysical Journal* **538** (2000) 473.
- [71] S. Brieden, H. Gil-Marín and L. Verde, *ShapeFit: extracting the power spectrum shape information in galaxy surveys beyond BAO and RSD*, *JCAP* **2021** (2021) 054 [2106.07641].
- [72] K.S. Dawson, D.J. Schlegel, C.P. Ahn, S.F. Anderson, É. Aubourg, S. Bailey et al., *THE BARYON OSCILLATION SPECTROSCOPIC SURVEY OF SDSS-III*, *Astron. J.* **145** (2012) 10.
- [73] D.J. Eisenstein, D.H. Weinberg, E. Agol, H. Aihara, C. Allende Prieto, S.F. Anderson et al., *SDSS-III: Massive Spectroscopic Surveys of the Distant Universe, the Milky Way, and Extra-Solar Planetary Systems*, *Astron. J.* **142** (2011) 72 [1101.1529].
- [74] A.J. Ross, W.J. Percival, A.G. Sánchez, L. Samushia, S. Ho, E. Kazin et al., *The clustering of galaxies in the SDSS-III Baryon Oscillation Spectroscopic Survey: analysis of potential systematics*, *Mon. Nat. Roy. Astron. Soc.* **424** (2012) 564 [1203.6499].
- [75] K.S. Dawson, J.-P. Kneib, W.J. Percival, S. Alam, F.D. Albareti, S.F. Anderson et al., *THE SDSS-IV EXTENDED BARYON OSCILLATION SPECTROSCOPIC SURVEY: OVERVIEW AND EARLY DATA*, *Astron. J.* **151** (2016) 44.
- [76] M.R. Blanton, M.A. Bershad, B. Abolfathi, F.D. Albareti, C. Allende Prieto, A. Almeida et al., *Sloan Digital Sky Survey IV: Mapping the Milky Way, Nearby Galaxies, and the Distant Universe*, *Astron. J.* **154** (2017) 28 [1703.00052].
- [77] J.E. Bautista, M. Vargas-Magaña, K.S. Dawson, W.J. Percival, J. Brinkmann, J. Brownstein et al., *The SDSS-IV Extended Baryon Oscillation Spectroscopic Survey: Baryon Acoustic Oscillations at Redshift of 0.72 with the DR14 Luminous Red Galaxy Sample*, *Astrophys. J.* **863** (2018) 110 [1712.08064].
- [78] H. Gao, Y.P. Jing, Y. Zheng and K. Xu, *Constructing the Emission-line Galaxy-Host Halo Connection through Auto and Cross Correlations*, *Astrophys. J.* **928** (2022) 10 [2111.11657].
- [79] M. Colless, G. Dalton, S. Maddox, W. Sutherland, P. Norberg, S. Cole et al., *The 2dF Galaxy Redshift Survey: spectra and redshifts*, *Mon. Nat. Roy. Astron. Soc.* **328** (2001) 1039 [astro-ph/0106498].
- [80] P. Zarrouk, E. Burtin, H. Gil-Marín, A.J. Ross, R. Tojeiro, I. Pâris et al., *The clustering of the SDSS-IV extended Baryon Oscillation Spectroscopic Survey DR14 quasar sample: measurement of the growth rate of structure from the anisotropic correlation function between redshift 0.8 and 2.2*, *Mon. Nat. Roy. Astron. Soc.* **477** (2018) 1639 [1801.03062].
- [81] A.J. Ross, J. Bautista, R. Tojeiro, S. Alam, S. Bailey, E. Burtin et al., *The Completed SDSS-IV extended Baryon Oscillation Spectroscopic Survey: Large-scale structure catalogues for cosmological analysis*, *Mon. Nat. Roy. Astron. Soc.* **498** (2020) 2354 [2007.09000].
- [82] A. Brodzeller, K. Dawson, S. Bailey, J. Yu, A.J. Ross, A. Bault et al., *Performance of the Quasar Spectral Templates for the Dark Energy Spectroscopic Instrument*, *Astron. J.* **166** (2023) 66 [2305.10426].
- [83] D.M. Alexander, T.M. Davis, E. Chaussidon, V.A. Fawcett, A. X. Gonzalez-Morales, T.-W. Lan et al., *The DESI Survey Validation: Results from Visual Inspection of the Quasar Survey Spectra*, *Astron. J.* **165** (2023) 124 [2208.08517].

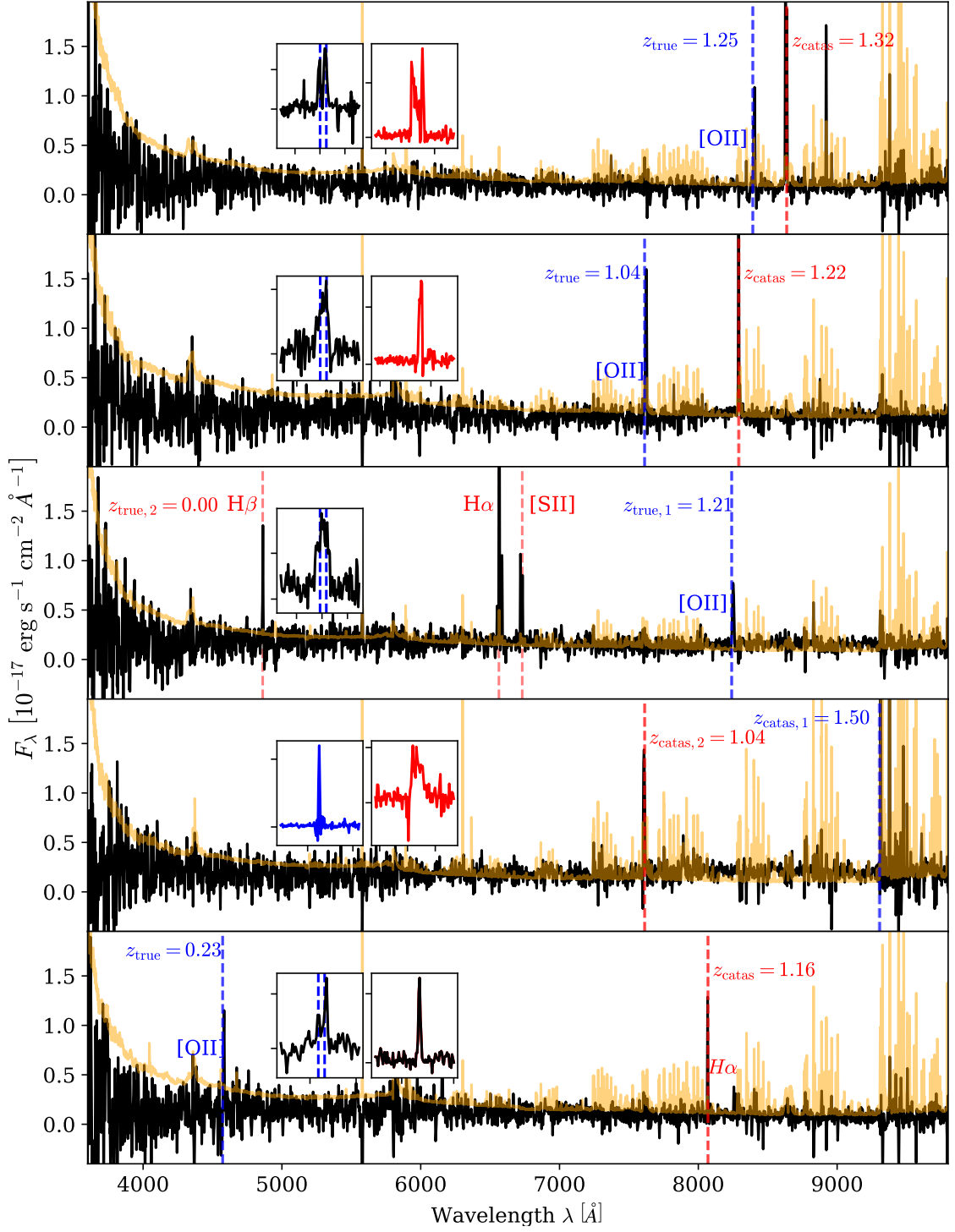


Figure 13. Five ELG spectra that suffer from catastrophics in redshift measurements due to the sky confusion at $z_{\text{catas}} \approx 1.32$, other sky confusion patterns, double objects in the spectrum, total failures in the redshift measurement, and the other failures like the misidentification of H α to be [O II]. The calibrated and sky-subtracted spectra are in solid lines. The orange shades in the foreground indicate the sky spectra. The blue vertical lines with z_{true} and [O II] labels indicate the true [O II] emissions positions except for the fourth spectra, in which the blue line indicates the sky residuals misidentified as [O II]. The zoom-in spectra in their vicinity are presented in the inserted subplot on the left-hand side. The red vertical lines with z_{catas} point out the position of features misidentified as [O II] line, except for the third spectra. Their enlarged features are the right-hand side inserted subplots. In the third spectra, there are H β , H α , [S II] to determine the redshift of the second object to be $z_{\text{true},2} = 0$.

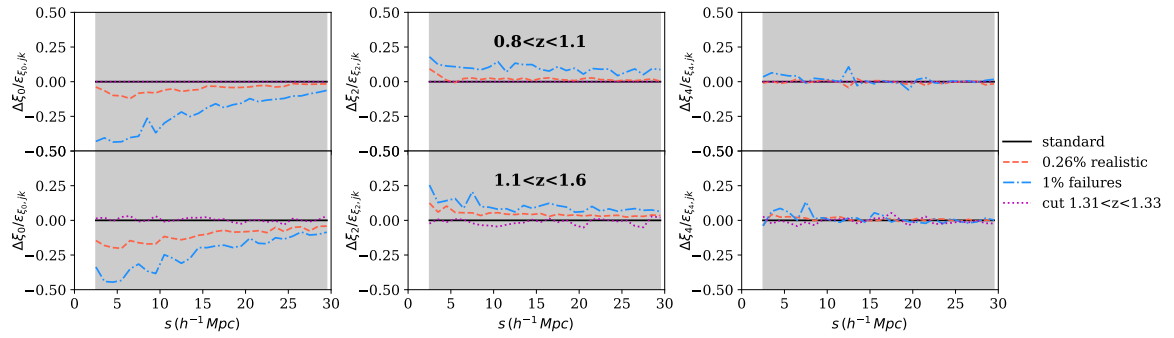


Figure 14. Similar to Figure 5 but for the comparison between the standard ABACUSSUMMIT galaxy mocks and the catastrophics-contaminated mocks with 0.26% realistic catastrophics (dashed lines), 1% random catastrophics (dash-dotted lines) and no ELGs at $1.31 < z < 1.33$ (dotted lines) at $s < 30 h^{-1}$ Mpc. The grey regions are the analytical $1\text{-}\sigma$ error of the ELG clustering. The impact of catastrophics at $1.1 < z < 1.6$ can be as large as $\sim 0.5\epsilon_{i,j}$, but is much smaller at $0.8 < z < 1.1$.